Modeling surface water and groundwater mixing and mixing-dependent denitrification with bedform dynamics

Xue Ping[1], Zhang Wen[1, 2*], Yang Xian[1], Menggui Jin[1, 2], Stefan Krause[3]

Revised manuscript submitted to *Hydrology and Earth System Sciences*

[1]Hubei Key Laboratory of Yangtze Catchment Environmental Aquatic Science, School of Environmental Studies, China University of Geosciences, Wuhan, China

[2]State Key Laboratory of Biogeology and Environmental Geology, China University of Geosciences, Wuhan, China

[3]School of Geography, Earth and Environmental Sciences, University of Birmingham, UK

*Corresponding author: Zhang Wen (wenz@cug.edu.cn)

16 **Notation**

S	Stream slope [-]
H	Water depth [L]
U	Stream velocity [L T^{-1}]
λ	Ripple wavelength [L]
u_c	Bedform migration celerity [L T^{-1}]
l	Streambed height [L]
H_d	Ripple height [L]
B	Riverbed per unit width [L]
D_{50}	Median sediment size [L]
x	Horizontal coordinate, rightward positive [-]
y	Vertical coordinate, upward positive [-]
k	Sediment permeability [L^2]
K	Sediment hydraulic conductivity [L T^{-1}]
h	Hydraulic head [L]
h_m	Amplitude of the sinusoidal head variation [L]
m	Wavenumber of the variation [-]
g	Gravity acceleration [L T^{-2}]
c_i	Concentration of reactive components [M L^{-3}]
c_{gw}	Groundwater tracer [M L^{-3}]
v	Seepage velocity [L T^{-1}]
v_i	Seepage velocity in the i-direction [L T^{-1}]

v_j	Seepage velocity in the *j*-direction [L T^{-1}]
θ	Sediment porosity [-]
α_L	Longitudinal dispersivity [L]
α_T	Transverse dispersivity [L]
D_{ij}	Hydrodynamic dispersion [L^2 T^{-1}]
D_m	Molecular diffusion coefficient [L^2 T^{-1}]
ι	Tortuosity factor [-]
V_{AR}	Maximum reaction rate of aerobic respiration [T^{-1}]
V_{DN}	Maximum reaction rate of denitrification [T^{-1}]
K_{inh}	Non-competitive inhibition factor [M L^{-3}]
K_{DOC}	Half-saturation for dissolved organic carbon [M L^{-3}]
K_{NO3^-}	Half-saturation for nitrate [M L^{-3}]
K_{O2}	Half-saturation for oxygen [M L^{-3}]
X_{AR}	Microbial concentration facilitating aerobic respiration [M L^{-3}]
X_{DN}	Microbial concentration facilitating denitrification [M L^{-3}]
ρ_s	Sediment density [M L^{-3}]
ρ	Water density [M L^{-3}]
P	Hydraulic pressure [M $L^{-1}T^{-2}$]
D^*	Dimensionless particle parameter [-]
u^*	Bed shear velocity [L T^{-1}]
u_{cr}^*	Critical bed shear velocity [L T^{-1}]
n	Manning coefficient [-]

τ^*	Shield parameter [-]
τ_{cr}	Critical shear stress [M $L^{-1}T^{-2}$]
τ_{cr}^*	Critical Shield parameter [-]
r	Submerged specific gravity of sediment [-]
R_{O2}	Aerobic respiration rate [M $L^{-3}T^{-1}$]
$R_{s\text{-}NO3}$	Non-mixing-dependent denitrification rate [M $L^{-3}T^{-1}$]
$R_{g\text{-}NO3}$	Mixing-dependent denitrification rate [M $L^{-3}T^{-1}$]
R_{DOC}	Dissolved oxygen carbon consumption rate [M $L^{-3}T^{-1}$]
υ	Kinematic viscosity of water [L^2 T^{-1}]
μ	Dynamic viscosity of water [M L^{-1} T^{-1}]
u_s	Underflow seepage velocity induced by stream gradient [L T^{-1}]
Re	Reynolds number [-]
U_r	ratio of bedform celerity to pore water velocity [-]
u_p	Darcy velocity induced by pumping process [L T^{-1}]
u_q	Vertical groundwater flux [L T^{-1}]
U_b	Ratio of vertical groundwater flux to hyporheic exchange flux
τ_R	Biogeochemical reaction timescale [T]
τ_T	Water transport timescale [T]
Da	Damköhler number [-]
Δx	Bedform migrating displacement per timestep (L)
dt	The length of per timestep (T)
Da'	Conversion factor for unit Darcy to m^2 [-]

F_{mix}	Proportion of mixing flux to hyporheic exchange flux [-]
A_{mix}	Proportion of mixing zone to the whole domain [-]
A	Streambed area [L^2]
M_{NDN}	Nitrate removed by non-mixing-dependent denitrification [M T^{-1}]
M_{DN}	Nitrate removed by mixing-dependent denitrification [M T^{-1}]
N_{RE}	Nitrate removal efficiency [-]
M_{in}	Nitrate being introduced into streambed [M T^{-1}]
Fin	Oxygen influx [M L^{-2} T^{-1}]
$Fout$	Oxygen outflux [M L^{-2} T^{-1}]
Ao	Oxygenated area [L^2]

Abbreviations

HZ	Hyporheic zone
SW	Surface water
GW	Groundwater
HEF	Hyporheic exchange flow
MF	Mixing flux
NMD	Non-mixing-dependent
MD	Mixing-dependent
AR	Aerobic respiration
DN	Denitrification
RMSE	Root means square error

DNRA	Dissimilatory nitrate reduction to ammonium
ANAMMOX	Anaerobic ammonium oxidation

17

Abstract The hyporheic zone (HZ), where surface water (SW) and groundwater (GW) interact and mix, acts as a critical interface that attenuates contaminants through enhanced biogeochemical cycling. While bedform migration significantly influences hyporheic exchange and non-mixing-driven reactions of solutes from upstream SW, the effects of bedform migration on SW-GW mixing dynamics and mixing-triggered biogeochemical reactions—particularly under gaining stream conditions—remain poorly understood. Establishing a coupled hydrodynamic and reactive transport model that incorporates bedform migration, this paper systematically examines nitrogen processing for scenarios of variable sediment grain size, stream velocities, and upwelling GW fluxes. Results of this study reveal that SW-GW mixing and mixing-triggered denitrification zones progressively transition from crescent shapes into uniform band-like configurations as bedforms migrate. Both hyporheic exchange flux and mixing flux increase with increasing stream velocity and associated bedform celerity. The mixing proportion and mixing zone size increase at the start of migration, while they reach approximately stable when turnover becomes the dominant hyporheic exchange mechanism. Slow to moderate migrated bedforms with enhanced mixing dynamics facilitate mixing-triggered denitrification, whereas fast stream flows and migrating bedforms shorten solute residence timescales and limits denitrification potential. Consequently, in fine to medium sandy sediments, groundwater-borne nitrate removal efficiency declines significantly with bedform migration. The self-purification capacity of the HZ, and particularly its functioning as a natural barrier against GW contamination, is hindered under such dynamic bedform conditions. These findings highlight the need to maintain stable bedform conditions in restoration projects to enhance the capacity of HZ contaminant attenuation.

1. Introduction

Anthropogenic activities such as the intensification of agricultural practices with its increased used of mineral and organic fertilizers, together with high livestock densities and emissions of inadequately treated domestic and industrial wastewater have significantly increased nitrogen loading to rivers and groundwater, which impacts water quality, causing eutrophication, hypoxic and related deterioration of ecosystem functions (Conley et al., 2009; Rouse et al., 1999). Long-term regulatory monitoring data (e.g., from the UK) indicate that nitrate levels have stabilized in many rivers, while nitrate concentrations in groundwater-fed rivers continue to increase (Burt et al., 2011; Howden and Burt, 2008). The persistence of nitrate contamination in groundwater and associated risks of a "nitrate time bomb" (Ascott et al., 2019) has highlighted the urgency of exploring the potential of natural microbial processes to mediate nitrate transformation and removal in riverbed sediments (Shelley et al., 2017; Lansdown et al., 2015; Rivett et al., 2008).

The hyporheic zone (HZ) has received significant attention for its potential to facilitate enhanced nitrate transformation and removal via denitrification that is a primary process permanently reducing nitrate, with hyporheic exchange flows (HEFs) acting as a critical mechanism for transporting nitrate-rich surface water to the riverbed sediments where microbial activities and biogeochemical reaction rates are enhanced (Boano et al., 2014; Boulton et al., 1998; Cardenas, 2015; Xian et al., 2022; Krause et al., 2022). It has for long been assumed that predominantly stream waters provide inputs of bioavailable (mainly dissolved) organic carbon (DOC), oxygen (O_2) and nitrate (NO_3^-) into the riverbed where the residence and reaction times determine the occurrence of aerobic respiration and the potential for shifts into anaerobic

conditions that may facilitate denitrification along the HEF paths in the presence of enough remaining DOC (Zarnetske et al., 2011a, b). These hydrological and biogeochemical mechanisms are in this form mainly representative of headwater streams, where the HEF is induced by stream flow turbulence (Boano et al., 2011; Roche et al., 2018, 2019), local geomorphological setting (Cardenas et al., 2008; Marzadri et al., 2012; Tonina and Buffington, 2007), and flow obstacles such as woody debris, streambed engineering or restoration structures (Briggs et al., 2013; Wondzell et al., 2009), and hyporheic nitrate removal processes expected to mainly occur at the middle to end- hyporheic flow paths within HEF cell sediments.

In lowland systems, groundwater-fed streams and rivers in permeable catchments will be dominated by base flow of often nitrate enriched groundwaters. The subsurface hydrological conditions are driven by horizontal HEF as well as vertical fluxes resulting from regional groundwater flow toward (or from) the stream. Spatial variability in regional groundwater flow can significantly affect hyporheic exchange and biogeochemical cycling (Boano et al., 2013; Krause et al., 2013; Munz et al., 2011; Naranjo et al., 2015). It is important to note that the groundwaters of many piedmont plains and lowlands are often contaminated with high nitrate concentrations, but usually low in bio-available DOC (Krause et al., 2022). When nitrate-rich groundwater upwells through deeper sediments and reaches a region enriched in availability of DOC, nitrate reduction processes are significantly facilitated in the condition (Krause et al., 2009; Naranjo et al., 2015; Ping et al., 2023; Trauth et al., 2017). Stelzer and Bartsch (2012) developed such a conceptual framework of nitrate-rich gaining fluvial setting from 8 sites in the Waupaca River Watershed with three order magnitude in groundwater nitrate concentration. Lansdown et al. (2014) also measured high denitrification rate at deep sediment in the coarse-

grained sediments typical of groundwater-fed system, located within the River Leith (Cumbria, UK) where diverse nitrogen concentration changes were confirmed earlier (Krause et al., 2009).

Turnover and removal of the large amounts of NO_3^- from groundwater require DOC either from autochthonous streambed sources or from downwelling surface water to stimulate nitrate reduction (Krause et al., 2013, 2022; Ping et al., 2023; Sawyer, 2015; Trauth et al., 2017). For coarse grain or sandy riverbeds with low autochthonous organic matter content, stream-borne DOC dominates the supply of carbon sources for nitrogen transformation processes. Sandy sediments with less autochthonous organic carbon sources covering the majority of alluvial riverbeds are commonly characterized by topographical features such as ripples, dunes, and riffle-pool sequenced. The typical and multiple HEF cells induced by bedform topography are generally in crescent shapes (Fox et al., 2014; Wu et al., 2024). The downward advection of stream borne DOC provides electron donor and mixes with nitrate-rich and anoxic groundwater. It has been shown that the highest potential for mixing triggered denitrification is often found at the margin of the HEF cells, which represents the last natural protection before nitrate enter a stream (Hester et al., 2013, 2014; Gu et al., 2008; Nogueira et al., 2022).The effects of mixing triggered denitrification on groundwater borne nitrate transformation in HZs have been studied almost exclusively for the case of stationary, that is immobile bedforms (Hester et al., 2017, 2019; Trauth and Fleckenstein et al., 2017; Ping et al., 2023).

Bedforms are mobile in dynamic equilibrium or undergo constant changes during periods of moderate to high stream flow, and they are typically found in medium and larger waterways under realistic field conditions (Bartholdy et al., 2015; Risse-Buhl et al., 2023; Schindler et al., 2015). For example, Harvey et al. (2012) observed the migrating bedforms of dunes (with a

106 median grain size D_{50} of 380 μm for the riverbed sediments) at a velocity of 57.6 cm/h during
107 base flow in the "Clear Run" stream in eastern North Carolina, USA. Ahmerkamp et al. (2017)
108 found that the ripple bedforms for sands (D_{50} = 63 μm) ranged from 11 to 29 cm with a constant
109 ratio of bedform height and length at 1/9, and migrated at velocities of 0.7–6.5 cm/h in the
110 German Bight, Southeastern part of the North Sea. Bedforms migration complicates the
111 development of hyporheic flow fields, facilitates solute exchange, alters redox conditions in
112 riverbeds, and affects contaminant transport and transformation (Ahmerkamp et al., 2015;
113 Schulz et al., 2023; Peleg et al., 2024). Previous studies focused on ripple-driven hyporheic
114 exchange in headwater to midstream reaches under neutral conditions, and simulated bedform
115 migration via a moving frame of reference (Ahmerkamp et al., 2015; Jiang et al., 2022; Kessler
116 et al., 2015; Zheng et al., 2019). Ping et al. (2022) used a fixed reference frame and noted that
117 bedform migration negatively impacts non-mixing-dependent denitrification rates and stream-
118 borne nitrate removal efficiency. However, no studies have yet investigated the effects of
119 bedform migration on surface water-groundwater mixing in the lowland reaches of streams
120 under gaining conditions, nor have they explored its controls or implications for mixing-induced
121 denitrification in groundwater-fed streams and rivers.

122 In this study, numerical modeling of hyporheic flow and multi-component solute (DOC,
123 O_2, and NO_3^-) transport is used to evaluate the effect of bedform migration on mixing-
124 dependent denitrification in the HZ of a gaining river, where the overlying stream water is
125 induced into the sediment by ripple-type bedforms. The objectives of this study are to determine
126 the effects of bedform migration on the overall extent and magnitude of mixing of surface water

and upwelling groundwater, as well as its influences on groundwater-borne nitrate transport and transformation.

2. Methods

2.1 Model description

The stream flow over the bedform generates head gradients along the riverbed surface, drives hyporheic exchange, and induces the formation of periodic ripples. Ripples develop and migrate downstream above the riverbed surface as a consequence of bedload transport, with sediment grain eroded and deposited at the surface, whereas deeper streambed sediments remain relatively stable (Harvey et al., 2012; Precht et al., 2004). From the perspective of an observer who stands at the target single riverbed and watches the ripples passing by, the bedform shapes and associated pressure profiles migrate downstream over the immobile riverbed layer. Because ripple heights (H_d = 2 cm) accounts for 20% of the stream water depth (H = 10 cm) and are far smaller than that of the underlying immobile domain (l = 16 cm), the undulating riverbed can be reasonably approximated as a flat bed with time-varying pressure patterns during bedform migration. Besides, reactive solute transport also primarily takes places within the immobile riverbed sediment. Therefore, a two-dimensional (2D) rectangular domain is constructed with a length (λ) of 0.2 m and depth (l) of 0.16 m. A fixed reference frame is adopted, with its origin located at the bottom-left corner of the model. Here, the horizontal direction corresponds to the x-axis and the vertical direction to the y-axis. The model domain has four corners: A (0, 0), B (0, l), C (λ, l), and D (λ, 0). The lateral boundaries are AB (left, x = 0) and CD (right, x = λ); the top boundary is BC (y = l), and the bottom boundary is AD (y = 0).

The model schematic is sketched in Figure 1. The model is relevant to the model used by Ping et al. (2022) but with significant differences. Specifically, Ping et al. (2022) focused on ripple-driven hyporheic exchange processes in the headwater to midstream sections of streams under neutral conditions. In contrast, the present study focuses on the downstream sections of rivers under gaining conditions, aiming to simulate surface water-groundwater interacting and mixing processes under dynamic bedforms. To our knowledge, previous migrating ripple models have extensively examined surface water-groundwater interaction processes (i.e., ripple-driven hyporheic exchange processes), yet the mixing process remains uninvestigated (Ahmerkamp et al., 2017; Jiang et al., 2022; Zheng et al., 2019; Kessler et al., 2015). In downstream sections, groundwater is typically nitrate-contaminated, and denitrification is often co-regulated by both mixing regimes. The model is also developed with advancements of these previous models by including an important biogeochemical reaction in nitrate dynamics, that is mixing-triggered denitrification (see next section for details).

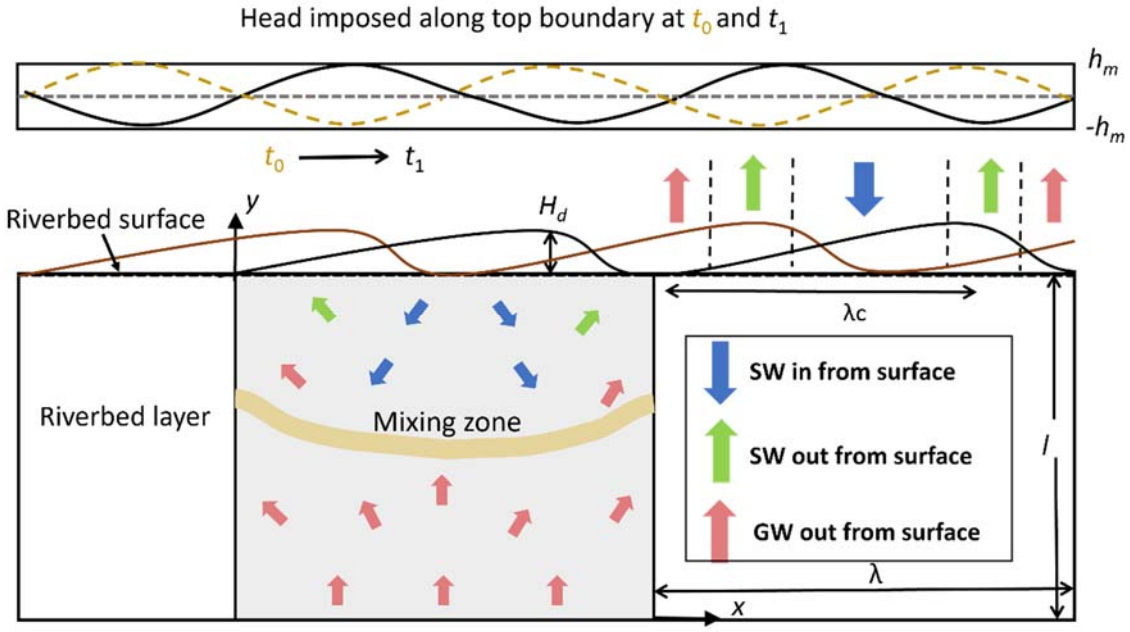

Figure 1. Schematic of the model domain with bed form geometry. Stream flow and bedform

163 migration are from left to right. The dashed yellow lines represent the streambed surface and
164 head profile at time t_0, and the solid black lines represent the streambed surface and head profile
165 after migration at t_1. “SW in” is where surface water enters the riverbed layer, “SW out” is
166 where surface water discharges to the stream, and “GW out” is along the upstream and
167 downstream sides of bedforms where groundwater discharges to the stream. The yellow band
168 represents the mixing zone of surface water and groundwater. NMD reaction = non-mixing-
169 dependent reaction and MD reaction = mixing-dependent reaction. This figure is modified from
170 Figure 2 in Ping et al. (2022), with permission granted by Wiley.

171 In this study, hyporheic flow, multi-component solutes (DOC, O_2, and NO_3^-) transport, and
172 biogeochemical reactions (both non-mixing-dependent NMD and mixing-dependent MD
173 reactions) are modelled in saturated sediments beneath a riverbed layer. Stream flow over the
174 riverbed is not simulated. The hyporheic exchange flow is driven by pumping (overlying flow
175 over the bed form produces a pressure~~hydraulic~~ head $h|_{y=l}$) and bedform migration (triangular
176 shaped ripples migrate downstream by an average velocity u_c) and influenced by upwelling
177 groundwater. Stream water transports DOC, O_2, and NO_3^- into the riverbed, whereas
178 groundwater polluted with NO_3^- upwells toward the stream. In order to distinguish NMD and
179 MD denitrification, we define stream-borne nitrate (s-NO_3^-) and groundwater-borne nitrate (g-
180 NO_3^-) as two distinct reactants.

181 **2.2 Model formulation**

182 2.2.1 Governing equation

183 The pore water flow was calculated using Darcy’s law and the groundwater flow equation:

$$\nabla\cdot\left(-K\nabla h\right)=0 \tag{1}$$

where h [L] is the pressure~~hydraulic~~ head, and K [L T^{-1}] = $k\rho g/\mu$ is the hydraulic conductivity, k [L^2] is the permeability of the riverbed, ρ [M L^{-3}] are the density of water, g [L T^{-2}] is the gravity acceleration, and μ [M L^{-1} T^{-1}] is the dynamic viscosity of water.

The transport of reactive solutes within the streambed sediment was described by the advection-dispersion-reaction equation:

$$\frac{\partial c_i}{\partial t}-\nabla\cdot\left(D_{ij}\nabla c_i\right)+\nabla\cdot\left(\boldsymbol{v}c_i\right)=R_i \tag{2}$$

where c_i [M L^{-3}] represents the concentration of reactive components, $\boldsymbol{v}$ [L T^{-1}] is the seepage or linear pore water velocity vector, D_{ij} [L^2 T^{-1}] is the hydrodynamic dispersion tensor, and R_i [M L^{-3}T^{-1}] denotes the biogeochemical rate of reactive components; the elements of the dispersion tensor D_{ij} are defined by Bear and Verruijt (1998):

$$D_{ij}=\left(\alpha_L-\alpha_T\right)\cdot\frac{v_i v_j}{|\boldsymbol{v}|}+\delta_{ij}\cdot\left(\alpha_T|\boldsymbol{v}|+\theta\cdot\imath D_m\right) \tag{3}$$

where α_L [L] and α_T [L] are longitudinal and transverse dispersivities, respectively, D_m [L^2 T^{-1}] is molecular diffusion coefficient, v_i and v_j denote the seepage velocities in the i-direction and j-direction, respectively; and $\imath$ [-] is tortuosity.

The biogeochemical reactions: aerobic respiration (AR), non-mixing-dependent, and mixing-dependent denitrification (DN) are considered in the reactive transport model:

$$AR: CH_2O+O_2\rightarrow CO_2+H_2O \tag{R1}$$

$$DN: CH_2O+0.8NO_3^-+0.8H^+\rightarrow CO_2+1.4H_2O+0.4N_2 \tag{R2}$$

Equations R1 and R2, with DOC as the electron donor and O_2 and NO_3^- as sequential electron acceptors, capture the primary mechanism of NO_3^- cycling and are widely used in studies on hyporheic zone nitrogen dynamics (Bardini et al., 2012; Hester et al., 2019; Zheng et al., 2019). Denitrification is the well-recognized critical process for NO_3^- transformation and reduction in riparian and hyporheic zones. The reaction stoichiometry and electron acceptor utilization order in R1 and R2 match well-established principles from lab incubations and field investigations (Hedin et al., 1998; Liu et al., 2017; Zarnetske et al., 2011a, 2011b). Dissimilatory nitrate reduction to ammonium (DNRA) and anaerobic ammonium oxidation (ANAMMOX) are not included in the model, as these processes play secondary role on nitrogen cycling and require highly specific conditions to occur (Zarnetske et al., 2012). Ammonia (NH_4^+) was excluded, as it is unstable in the study environment: NH_4^+ in surface water or groundwater is prone to nitrification (converting NH_4^+ to NO_3^-) either within hyporheic flow cells or in upwelling groundwater upon O_2 exposure, leading to relatively low NH_4^+ concentrations (Hester et al., 2014).

Reaction rates were defined using Monod kinetics (Monod, 1949):

$$R_{AR} = V_{AR} \times X_{AR} \times \frac{c_{O_2}}{c_{O_2} + K_{O_2}} \times \frac{c_{DOC}}{c_{DOC} + K_{DOC}} \tag{4}$$

$$R_{DN} = V_{DN} \times X_{DN} \times \frac{c_{NO_3^-}}{c_{NO_3^-} + K_{NO_3^-}} \times \frac{c_{DOC}}{c_{DOC} + K_{DOC}} \frac{K_{inh}}{K_{inh} + c_{O_2}} \tag{5}$$

The reaction terms R_i was given by

$$R_{s-NO_3^-} = -R_{DN}(c_{s-NO_3^-}) \tag{6}$$

$$R_{g-NO_3^-} = -R_{DN}(c_{g-NO_3^-}) \quad (7)$$

$$R_{O_2} = -R_{AR} \quad (8)$$

$$R_{DOC} = -R_{AR} - 0.8 \times (R_{DN}(c_{s-NO_3^-}) + R_{DN}(c_{g-NO_3^-})) \quad (9)$$

where V_{AR} and V_{DN} [T^{-1}] are the maximum reaction rate of AR and DN, X_{AR} and X_{DN} [$M\ L^{-3}$] are the biomass of functional microbial groups facilitating the reaction components of AR and DN. K_{inh} [$M\ L^{-3}$] is a non-competitive inhibition factor used for representing inhibition of DN given oxygen availability.

2.2.2 Boundary condition

The pressure~~hydraulic~~ head imposed along the top boundary was described as a sinusoidal function that moves downstream by the ripple migration velocity (u_c [$L\ T^{-1}$]; Boano et al., 2013):

$$h|_{y=l} = h_m \cdot \sin m(x - u_c dt) \quad (10)$$

where m [-] is the wave number of the variation ($m = 2\pi/\lambda$), dt [T] denotes a timestep in the simulation, and h_m [L] is the amplitude of the head variation (Elliott and Brooks, 1997):

$$h_m = a \frac{U^2}{2g} \left(\frac{H_d / H}{0.34} \right)^e \quad (11)$$

where $a = 0.28$ [-] is a dimensionless coefficient, U [$L\ T^{-1}$] is the average stream velocity, H_d [L] is the height of the ripple, H [L] is the water depth. The exponent e equals to 3/8 if $H_d < 0.34H$ and 3/2 otherwise. Given the periodic characteristics typically observed in riverbeds under field conditions (Ahmerkamp et al., 2017; Harvey et al., 2012), a single ripple was chosen in this study. Quasi-p~~P~~eriodic pressure and periodic solute boundary conditions were applied to side boundaries AB and CD to replicate the repetitive geometric constraints of the streambed. This is

a well-established practice in hyporheic exchange modeling, as it minimizes edge effects without the need for computationally intensive full-scale simulations of multiple consecutive bedforms:

$$P(0,y,t) = P(\lambda,y,t) + \Delta P \tag{12}$$

$$c_i(0,y,t) = c_i(\lambda,y,t) \quad \boldsymbol{n}\cdot\left(-D_{ij}\nabla c_i\right)\Big|_{x=0} = \boldsymbol{n}\cdot\left(D_{ij}\nabla c_i\right)\Big|_{x=\lambda} \tag{13}$$

where P [M $L^{-1}T^{-2}$] is the pressure calculated using the hydrostatic head from equation (10) and elevation, $P = \rho g(h+y)$. The additional pressure drop ΔP [M $L^{-1}T^{-2}$] was derived from the streambed gradient and calculated using $\Delta P = S\rho g\lambda$. For the validation of model generalization, simulation of three consecutive ripples was conducted. The middle ripple was focused on to compare its vertical boundary-related pressure and solute concentration with outcomes from the single-ripple model. Simultaneously, comparisons were made between the two models (single-ripple and three-consecutive-ripple) regarding simulated riverbed flow fields, nitrate plumes, influxes, and reaction rates. Although moderate left/right boundary pressure differences were detected between their simulation results, such variations had negligible effects on reactive solute transport. This comparison is provided in the Supporting Information (Text S2).

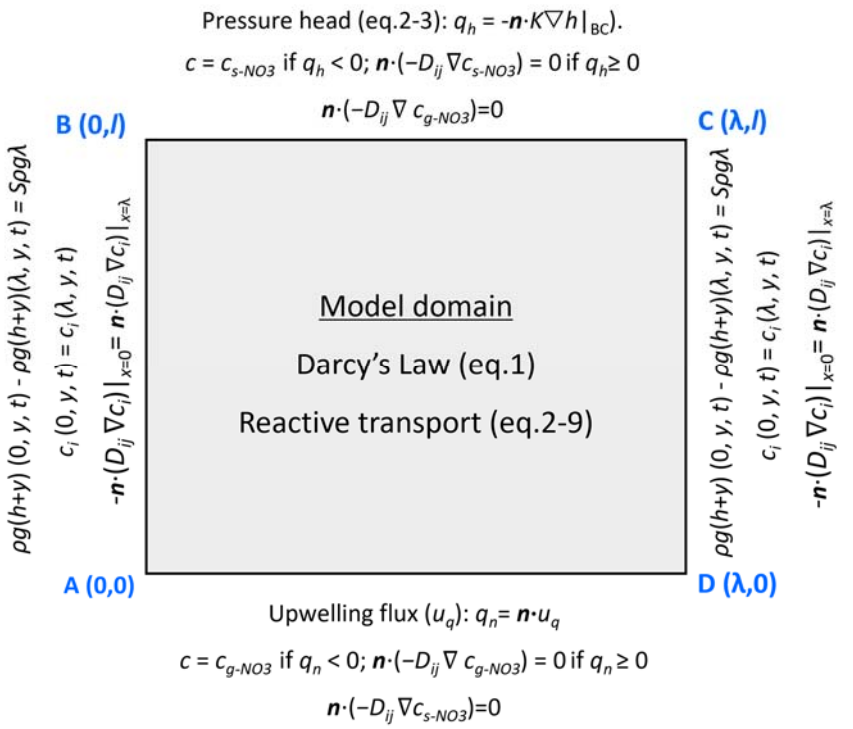

Figure 2. Schematic diagram of the simulated domain and boundary conditions.

At the bottom boundary, an upward groundwater flux was defined to mimic the process of groundwater discharge. For groundwater borne nitrate, the bottom boundary was specified as an open Dirichlet boundary with constant g-NO_3^- concentration in groundwater:

$$\begin{cases} c = c_i & \boldsymbol{n}\cdot\boldsymbol{v} < 0 \\ \boldsymbol{n}\cdot\left(-D_{ij}\nabla c_i\right) = 0 & \boldsymbol{n}\cdot\boldsymbol{v} \geq 0 \end{cases} \tag{14}$$

where the outward unit normal is *n*. Besides, the top boundary for the g-NO_3^- was assigned as outflow condition.

For stream-borne solutes includes DOC, O_2, and s-NO_3^-, an open boundary with a constant solute concentration was imposed on the top boundary, and outflow boundary was applied on the bottom of the domain. The concentrations of the all solutes were initially assumed to be zero. A quantitative mass-balance check for the model was included in Supporting Information

Text S2.

2.3 Bedform migration

In this study, ripples formation was qualitatively determined using the bedform stability diagram (Figure 3). This diagram is a summarized reference for examining equilibrium bed configurations in unidirectional flow, derived from a series of flume experiments and field studies (Ashley, 1990). Besides, a series of quantitative criteria (Text S1 in the supporting information: Criteria for ripple migration) was examined to ensure ripple formation under the modeled scenarios and the achievement of dynamic equilibrium. For a specific grain size of streambed sediment (D_{50}), particular stream velocities (U) satisfying all these criteria are selected and displayed in Figure 3. All simulation scenarios were listed in the Table S1.

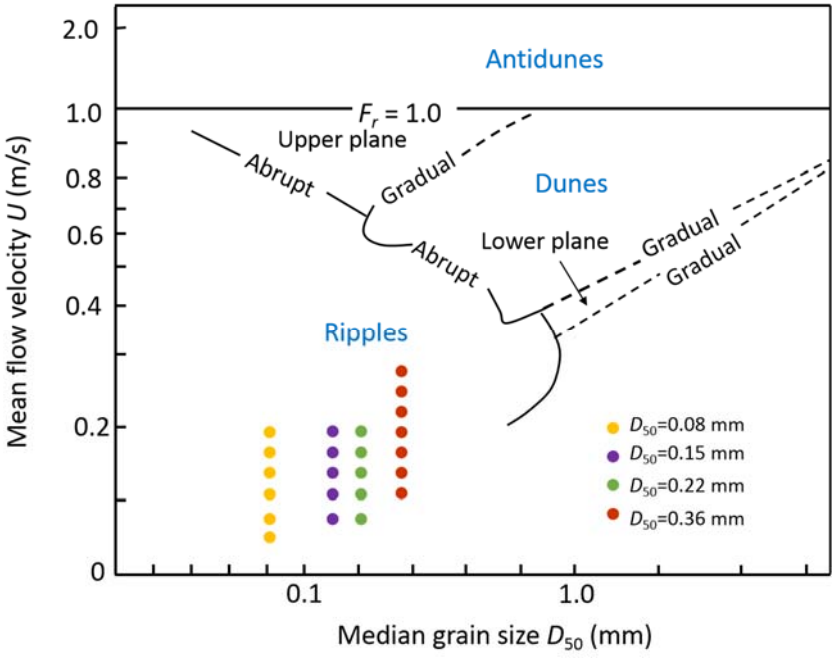

Figure 3. The bedform stability diagram (modified from Ashley, 1990) showing the bedform properties and hydraulic conditions considered in this study. Different colors indicate different median grain sizes of the streambed sediments. For each sediment grain-size scenario, various

streamflow conditions were simulated, corresponding to the velocity values shown on the *y*-axis

Ripple migration velocities were implemented using an empirical relation after Coleman and Melville (1994), which was derived from flume experiments:

$$\frac{u_c}{\left(u^* - u_{cr}^*\right)\left(\tau^* - \tau_{cr}^*\right)}\left(H_d / D_{50} - 3.5\right)^{1.3} = 40 \quad (15)$$

where $u^* = (gHS)^{0.5}$ [L T^{-1}] is the bed shear velocity, S [-] is the stream gradient and calculated by Chezy equation ($U = H^{2/3}S^{1/2}/n$, where n [-] is the Manning coefficient and assumed to be 0.02 for sand). u_{cr}^* [L T^{-1}] is the critical bed shear velocity and it can be calculated by the critical Shield parameter τ_{cr}^* ($\tau_{cr}^* = \tau_{cr} / g(\rho_s - \rho)D_{50}$, $u_{cr}^* = (\tau_{cr} / \rho)^{0.5}$, ρ_s [M L^{-3}] and ρ [M L^{-3}] are the density of sediment and water), and τ^* is the shield number related to the bed shear velocity ($\tau^* = u^{*2}/rgD_{50}$; r [-] is the submerged specific gravity of sediment = $(\rho_s - \rho)/\rho$). The critical shields parameter τ_{cr}^* defines the threshold for the initialization of motion, and it is determined by the dimensionless particle parameter D^* [-] (Soulsby, 1997; Zheng et al., 2019):

$$\tau_{cr}^* = \frac{0.3}{1 + 1.2D^*} + 0.055\left[1 - \exp\left(-0.02D^*\right)\right] \quad (16)$$

where $D^* = D_{50}\cdot(rg/\upsilon^2)^{1/3}$, υ is the kinematic viscosity of water [L^2 T^{-1}]; The derived celerity was substituted into Equation (10) to determine the migration of sinusoidal pressure head profile with ripples moving.

2.4 Governing non-dimensional numbers

The characteristics of the modeled system were depicted by a series of non-dimensional numbers, which represent the relative dominance of various forces, transport, and reaction processes in this system. Firstly, the Reynolds number *Re* was used to characterize the flow

condition of surface water (Cardenas and Wilson, 2006):

$$Re = \frac{UH_d}{\upsilon} \tag{17}$$

where υ [L^2 T^{-1}] represents kinematic viscosity of water.

The dimensionless parameter U_r [-] was introduced to represent the relative magnitude of bedform celerity and the pressure-induced pore water velocity driven by pressure variation over the ripple surface and upwelling groundwater:

$$U_r = \frac{\theta \cdot u_c - u_s}{u_p} \tag{18}$$

where u_s [L T^{-1}] is the seepage velocity of the underflow induced by stream gradient ($u_s = KS$), and thus the characteristic horizontal velocity is $u_c - u_s/\theta$. u_p/θ [L T^{-1}] is the pore water velocity induced by pumping process and is calculated using the analytical solution after Boano et al. (2009) and Fox et al. (2014) accounting for vertical groundwater flux (u_q [L T^{-1}]):

$$u_p = u_{p,0}\sqrt{1-\left(u_q/\pi u_{p,0}\right)^2} + \left(\left|u_q\right|/\pi\right)\sin^{-1}\left(\left|u_q\right|/\pi u_{p,0}\right) - \left(\left|u_q\right|/2\right) \tag{19}$$

$$u_{p,0} = a\frac{KU^2}{g\lambda}\left(\frac{H_d/H}{0.34}\right)^m \tag{20}$$

where $u_{p,0}$ [L T^{-1}] represents the hyporheic exchange solely driven by pressure variation over the sediment-water interface; if $U_r > 1$, turnover process dominates and controls the hyporheic exchange, otherwise, the system is pumping process dominated (Jiang et al., 2022).

The relative magnitude of hyporheic exchange flux driven by pressure variation along the riverbed surface and upwelling groundwater flux was determined as:

$$U_b = \frac{u_q}{u_{p,0}} \tag{21}$$

The relative dominance of hyporheic exchange and biogeochemical reaction in nitrate removal can be defined by the Damköhler number (Ocampo et al., 2006; Zarnetske et al., 2012; Zheng et al., 2019):

$$Da = \frac{\tau_T}{\tau_R} \tag{22}$$

the characteristic timescale for the transport of solutes through the ripple was estimated as (Azizian et al., 2015):

$$\tau_T = \frac{\lambda\theta}{\pi^2 u_p} \tag{23}$$

and the reaction timescale (τ_R) represents the time needed to consume dissolved oxygen of hyporheic water to a prescribed anoxic environment threshold (2 mg/L). The reaction timescale was described as:

$$\tau_R = \frac{\ln\left(c_{O_2}/c_{O_2,\lim}\right)}{V_{AR}} \tag{24}$$

biogeochemical reactions are transport-limited when $Da < 1$. The biogeochemical reactions depended on reaction kinetics due to the brevity of the time that reactants spend within the HZ. Under these low *Da* conditions, the HZ remains oxic conditions, resulting in a minimal or no denitrification to occur. Conversely, when $Da > 1$, the residence time of reactants exceeds the reaction time, and thus oxygen is consumed and favors for the occurrence of denitrification in anoxic conditions (Jiang et al., 2022; Zarnetske et al., 2011a).

2.5 Model setup and parametrization

All parameter values in this study were shown in Table 1. The bedform geometry of Ping et al. (2022) was adopted for this study (the ripples located at λ_c = 0.15 m with a height of H_d = 0.02 m). Here grain sizes D_{50} of 0.08, 0.15, 0.22 and 0.36 mm were considered, typically falling within characteristic grain diameters on sandy riverbeds (Ahmerkamp et al., 2017; Harvey et al., 2012). The permeability of riverbed was calculated using the empirical relation $k = Da' \times 735 \times 10^6 \times D_{50}^2$ (where $Da' = 9.869 \times 10^{-13}$ is the conversion factor for unit Darcy to m^2; Gangi, 1985).

The concentrations of DOC, O_2, and s-NO_3^- in stream were specified as 30 mg/L, 8 mg/L, and 5 mg/L. This configuration represents a pristine stream characterized by moderate nutrient levels (Ocampo et al., 2006). The g-NO_3^- in groundwater was set as 15 mg/L, representing the chemical signature of nitrate-contaminated groundwater that lacks both oxygen and organic matter (Hester et al., 2014). The maximum reaction rate and corresponding functional microbial concentration for AR and DN were listed in Table 1, the choose biogeochemical values are consistent with the parameter setting of nutrient cycling in hyporheic zones and riparian zones (Gu et al., 2008; Nogueira et al., 2021; Zarnetske et al., 2012).

Table 1. Model parameters used in numerical simulations

Parameter	Description	Value
l [m]	Streambed depth	0.16 [a, b]
l_c [m]	Ripple crest	0.15 [a, b]
λ [m]	Wavelength of ripple	0.2 [a, b]

H_d [m]	Height of ripple	0.02 [a, b]
H [m]	Stream water depth	0.1 [a, b]
θ [1]	Porosity	0.38 [e]
α_L [m]	Longitudinal dispersivity	0.01 [f]
α_T [m]	Transverse dispersivity	0.001 [f]
K_{inh} [mg L^{-1}]	Inhibition constant	0.25 [c, d]
K_{DOC} [mg L^{-1}]	Half-saturation constant for dissolved organic carbon	6 [c, d]
K_{NO3} [mg L^{-1}]	Half-saturation constant for nitrate	1 [c, d]
K_{O2} [mg L^{-1}]	Half-saturation constant for dissolved oxygen	0.5
V_{DN} [h^{-1}]	Maximum specific uptake rate for denitrification	1 [c, d]
V_{AR} [h^{-1}]	Maximum specific uptake rate for aerobic respiration	2 [c, d]
C_{DOC} [mg L^{-1}]	Concentration of dissolved organic carbon in stream	30
C_{O2} [mg L^{-1}]	Concentration of dissolved oxygen in stream	8
$C_{s\text{-}NO3^-}$ [mg L^{-1}]	Concentration of nitrate in stream	5
$C_{g\text{-}NO3^-}$ [mg L^{-1}]	Concentration of nitrate in groundwater	15

[a] Janssen et al. (2012) [b] Ping et al. (2022) [c] Zarnetske et al. (2012) [d] Sawyer (2015) [e] Ahmerkamp et al. (2015) [f] Bardini et al. (2012)

The following distinct model experiments were carried out: The Reynolds number, i.e., mean stream velocity, was varied for Re = 2000–6000 in intervals of 500, with corresponding stream water velocities of U = 0.1–0.3 m/s. The range of U_b was set from 0.3 to 0.7 in intervals of 0.1; correspondingly, the upwelling groundwater flux u_q was ranged between $0.3\times u_{p,0}$ and $0.7\times u_{p,0}$. A larger upward flux than $0.9\times u_{p,0}$ would eliminate the entire hyporheic flow cell, thus

363 the maximum boundary flux was set at a value slightly below this threshold. Meanwhile a
364 minimum of $0.2\times u_{p,0}$ ensures that upwelling groundwater is still mixing with surface water with
365 minor influences on hyporheic flow cell. Longitudinal and transverse dispersivities (α_L and α_T)
366 are important values for obtaining accurate mixing. Here sensitivity analysis of local dispersion
367 was conducted by varying α_L from 0.001 to 0.015 m, with α_T set to1/10 of α_L. Molecular
368 diffusion was fixed at 10^{-9} m^2/s, which has a secondary effect on solute dispersion process. This
369 sensitivity analysis is provided in the Supporting Information (Text S4).

370 The finite element software, COMSOL Multiphysics (version 6.1) was used to solve the
371 Darcy flow and multi-component solute transport model. Three computational grids were
372 evaluated to ensure grid resolution independence of simulated results, confirming that the grid is
373 sufficiently refined to capture mixing dynamics and minimize numerical dispersion. The fine,
374 base and coarse grid sizes were 1.5 mm, 2 mm, and 2.5 mm, respectively. The grid
375 independence analysis was provided in the Supporting Information (Text S2). For the
376 simulations, the base grid size was selected, with the domain discretized into 19,940 cells. To
377 maintain a constant bedform displacement (Δx) per timestep, the simulation was conducted with
378 Δx = 2 mm, while dt was adjusted in inverse proportion to the migration celerity u_c. The total
379 duration of the simulation was set to be equal to the time needed for hundreds of ripples to travel
380 across the modeled domain until the hyporheic exchange and biogeochemical processes reached
381 quasi-steady states.

2.6 Model Metrics

2.6.1 Mixing of surface water and groundwater

Here, macroscopic mixing is defined as the colocation of surface water (SW) and groundwater (GW) within a specific aquifer volume (e.g., a numerical model element or cell), a process that causes solutes to be present simultaneously in an overlapping region (Nogueira et al., 2022). There is no established standard for the threshold governing SW and GW fractions during the mixing process; nonetheless, the general recognition is that mixing occurs when the GW proportion falls within the range of 10% to 90% (Hester et al., 2013; Woessner et al., 2000). This interval effectively distinguishes the occurrence of mixing, where SW and GW interact dynamically, from the two endmembers: pure GW (>90%) and pure SW (<10%). To evaluate the influence of threshold variations on mixing metrics, sensitivity analysis was conducted to examine three alternative GW fraction ranges: 10%–90% (wider interval), 16%–84%, and 20%–80% (narrower range). Thus, mixing flux and mixing zone were calculated based on these three thresholds.

A constant concentration boundary condition of conservative tracer (c_{gw} = 1 mg/L) in GW was specified to represent the tracer signature of groundwater, following the methods outlined by Hester et al. (2013, 2014). The groundwater-borne tracer that undergoes mixing as it transitions from flow paths originating at the bottom boundary to those emerging at the streambed surface was quantified to determine the net effect of mixing. The streambed surface was divided into three zones (Figure 1): “SW IN”, where surface water enters the riverbed layer; “SW OUT”, where surface water discharges back into the overlying water column; and “GW OUT”, where upwelling groundwater discharges into the stream. The conservation tracer flux

for the SW OUT zone was used to describe mixing. If no mixing occurred, all the conservative tracer entering the model at the bottom boundary would exit through the GW OUT zone on the riverbed surface. The arrival of conservative solute at the riverbed surface is defined as the start of mixing, and the complete leave of all the conservation solute from the riverbed is defined as the end of mixing. Due to dispersion, the groundwater-borne tracer gradually spreads through the streambed and eventually crosses the sediment-water interface. The terms "mixing start and end" denote the period over which mixing is calculated.

The mixing flux across the riverbed surface was determined by integrating the outward volumetric flux containing groundwater-borne conservation solute within the specified concentration range (i.e., c_{gw} = 0.1–0.9 mg/L, c_{gw} = 0.16–0.84 mg/L, c_{gw} = 0.2–0.8 mg/L). This flux corresponds to groundwater flowing through "SW OUT" zone. Concurrently, the mixing zone was calculated by integrating the riverbed area that contains groundwater-borne conservation solute within the specified concentration range. The average mixing flux and mixing zone over the whole~~is~~ mixing period were computed and termed the mixing flux (*MF*) and mixing zone, respectively. The mixing fraction (*Fmix*) was computed as the ratio of the mixing flux to the total hyporheic flux, which was derived from integrating the volumetric flux along the sediment-water interface (including both SW OUT and GW OUT). *Fmix* serves as a metric to quantify the proportion accounted for by the SW-GW mixing flux within the overall flux of SW and GW interaction across the sediment-water interface. *Amix* is defined as the ratio of the mixing zone to the entire modeled domain, representing the proportion of the riverbed occupied by the mixing zone.

2.6.2 Nitrate reaction rate and efficiency

When the hydro-physical and biogeochemical conditions reach a quasi-steady state, the average flux of stream- or groundwater- borne nitrate entering the riverbed layer over the final serval periods of ripple migration was calculated:

$$M_{in,s-NO_3^-} = \frac{1}{w}\sum_T B\int \boldsymbol{v} c_{s-NO_3^-} - \theta D_{ij}\cdot\nabla c_{s-NO_3^-} dL_{top} \quad (25)$$

$$M_{in,g-NO_3^-} = \frac{1}{w}\sum_T B\int \boldsymbol{v} c_{g-NO_3^-} - \theta D_{ij}\cdot\nabla c_{g-NO_3^-} dL_{bottom} \quad (26)$$

where B [L] is the per unit width, θ [-] is the sediment porosity, and $w = T/dt$ [-]; L_{top} and L_{bottom} refer to the top boundary BC and bottom boundary AD, respectively.

The total amount of nitrate removed by NMD denitrification and MD denitrification were calculated as follows during the same time interval:

$$M_{NMD} = \frac{1}{w}\sum_T B\int R_{DN}(c_{s-NO_3^-})dA \quad (27)$$

$$M_{MD} = \frac{1}{w}\sum_T B\int R_{DN}(c_{g-NO_3^-})dA \quad (28)$$

where A [L^2] is the area of the streambed.

Nitrate removal efficiency was quantified as the rate of nitrate removed from the riverbed layer divided by the nitrate flux entering the riverbed layer:

$$N_{RE-NMD} = \frac{M_{NMD}}{M_{in,s-NO_3^-}}, \quad N_{RE-MD} = \frac{M_{MD}}{M_{in,g-NO_3^-}} \quad (29)$$

3. Results

3.1 Model validation

3.1.1 Validation of flat bed model with triangular ripple model

Model validation was conducted in two steps, with two numerical methods employed to represent moving bedforms. Beyond simulating porewater flow and reactive solute transport in a fixed frame of reference with a flat riverbed surface, a reference frame moving with triangular ripples was also adopted to capture bedform migration, following the methods of Bottacin-Busolin and Marion (2010), Ahmerkamp et al. (2015), and Kessler et al. (2015). The latter method captures bedform migration while preserving the ripple shape, and comparisons between the two approaches were conducted to examine the impact of neglecting ripple geometry on the simulated results.

A typical case (Re = 3000, U_b = 0.6 and D_{50} = 0.15 mm) was chosen here for comparison. The relative differences between these two modeling approaches were compared after normalizing the triangular ripple shape to a flat riverbed by projecting the values on the sloped edges onto the horizontal straight boundary. The overall patterns of pressure head, Darcy velocity, and stream-borne solute plume distributions were mostly similar (Figure 4). The difference in groundwater-borne nitrate plumes is attributed to the distinct advection velocities for reactive solute transport. Specifically, the moving reference frame involves a transformation of the horizontal coordinate system, based on the assumption that the frame of reference moves in the direction of bedform migration and at the same migration celerity; in this frame, the modeled advection velocity of reactive solutes is the seepage velocity minus the celerity. Thus,

in the triangular ripple model, g-NO_3^- flows upstream with larger advection velocities, resulting in a more uniform solute plume; in contrast, it exits the riverbed across the entire riverbed surface in the flat bed model (see the white streamlines). Correspondingly, discrepancies emerge in the crest area of the MD denitrification zone.

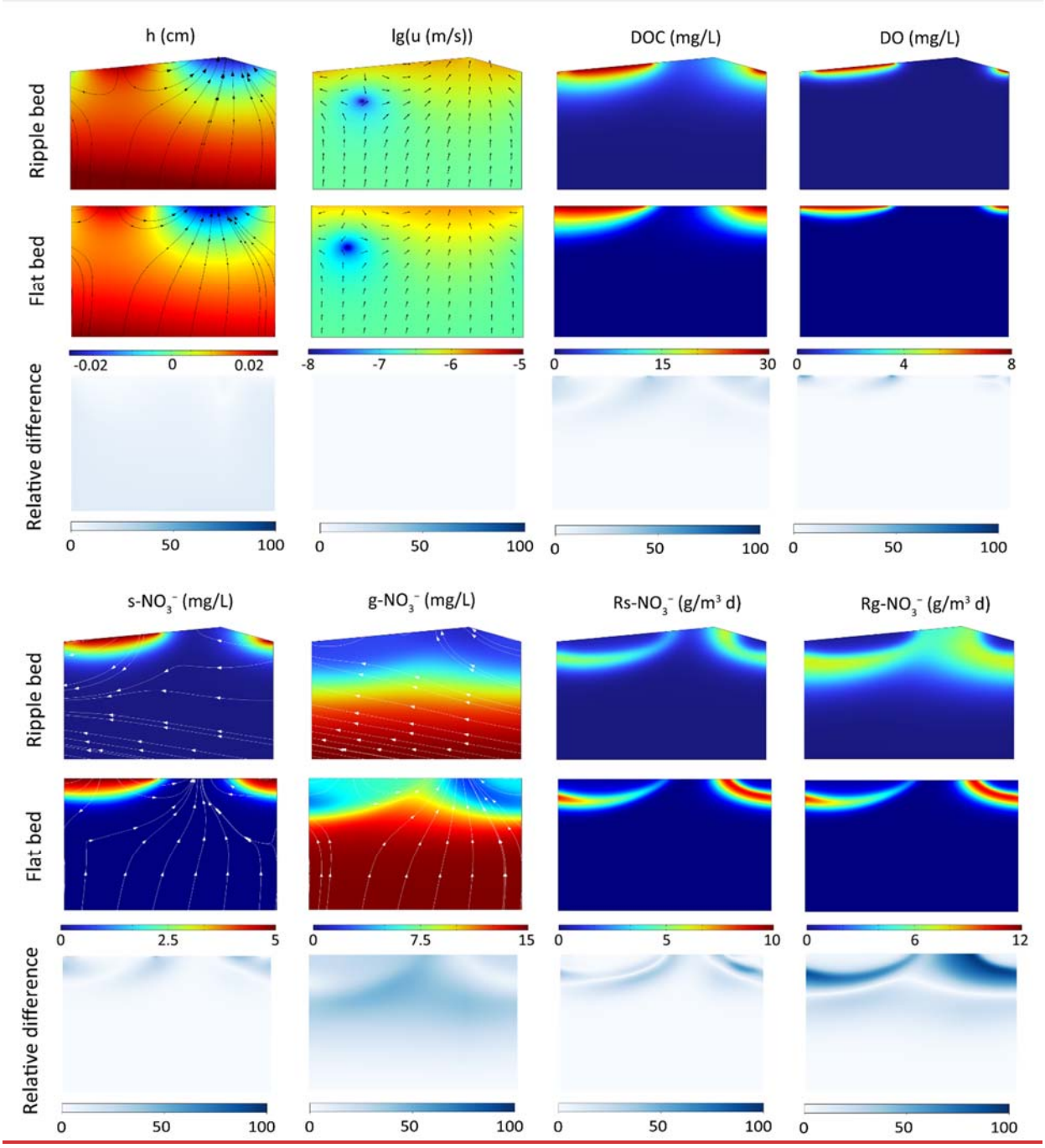

Figure 4. Comparison of hyporheic flow and reactive solute transport modeling results from the

468 flat bed model and the triangular ripple model. Streamlines and arrows in the Darcy flow field
469 indicate porewater flow, while streamlines in nitrate solute plumes represent the advection
470 velocity of reactive solute transport.

471 Compared with the triangular ripple model, the flat bed model ~~exhibit~~exhibits ~~slightly~~
472 larger hyporheic exchange flux, mixing flux, and stream-borne nitrate influx. The relative
473 difference ~~errors~~ are approximately 5~~10~~%. Meanwhile, both the total MD and NMD
474 denitrification rates are higher in the triangular ripple model than in the flat bed model, with
475 relative difference ~~errors~~ around 10%. Additionally, the spatial relative differences between
476 these two models are depicted in Figure 4. The relative difference is the absolute difference
477 between the values calculated by the two models at the same coordinate location divided by the
478 maximum value in the flat bed model. Note that the largest differences occur in the MD
479 denitrification hotspots. Spatially, the flat bed model captures the hotspots of the denitrifying
480 zone but underestimates the rates, potentially leading to an underestimation of groundwater
481 borne nitrate removal efficiency. ~~Differences in the results of the simulated domain cause subtle~~
482 ~~changes in flow and transport processes, changes that are acceptable for our intended purposes.~~
483 To further assess the differences between the two models and their reliability, two methods were
484 utilized to perform validation against the experiments by Wolke et al. (2020).

485 3.1.2 Validation of numerical models with laboratory experiments

486 The developed models were validated through comparison with Wolke et al.'s (2020) flume
487 experiments, which investigated the evolution of oxygen in the riverbed under varying
488 conditions of mean stream velocity (0.16−0.32 m/s) and bedform migration celerity (0−0.394
489 cm/h). The experiment was designed with a total of 5 operating conditions, each of which was

repeated twice and labeled as Set 1 and Set 2. Oxygen distribution within sediments was measured via planar optodes, and the oxygenated zone was defined as regions where oxygen saturation exceeds 15%. Oxygen consumption was observed within riverbed layer and aerobic respiration is widely recognized as the dominant process driving oxygen consumption within riverbed sediments (Ahmerkamp et al., 2017; Reeder et al., 2018). In their experiments, a fixed amount of NaCl was added to surface water; this NaCl was then used to compute hyporheic exchange flux (*HEF*) from the decline in its concentration, following the empirical equation~~method~~ by Fox et al. (2018). The oxygen influx (F_{in}) and outflux (F_{out}) were calculated by multiplying *HEF* by the surface water oxygen concentration and the mean oxygen concentration in the oxygenated zone, respectively.

Two numerical models: the flat bed model and the triangular ripple model, were developed under the same hydraulic conditions, with their parameters adjusted to fit *HEF*, F_{in}, F_{out}, and A_O to experimental data. The model parameters were summarized in Supporting Information Text S3: Model validation. All physical and hydraulic parameters (e.g., ripple geometry, streamflow, bedform migration velocity, porosity, and permeability) were used exactly as reported in Wolke et al. (2020) experiments without any adjustment. Only the biogeochemical reaction parameters (e.g., maximum oxygen consumption rate, and half-saturation constant for oxygen) were calibrated to match the observed oxygen plume, as these parameters are difficult to measure directly in dynamic streambed environments and are commonly calibrated in reactive transport models.

In the numerical model, *HEF* was calculated by integrating the volumetric flux over the inflow zones along the sediment-water interface. Oxygen transport was governed by the

advection-dispersion-reaction equation, where oxygen consumption occurred through aerobic respiration following the Monod kinetics described by Equation (8). The F_{in} and F_{out} were then computed by multiplying the *HEF* by the oxygen concentration in the surface water and the oxygen concentration over the outflow zones along the riverbed surface, respectively. The oxygenated area was calculated by integrating the riverbed portions where oxygen saturation exceeds 15%. Based on the criteria for ripple migration, it was determined that under the hydraulic conditions of Run 5, ripples could not migrate while maintaining their shapes due to increased stream flow velocity. Therefore, the model validation simulations considered four hydraulic conditions of Run 1 to 4.

~~The model parameters used and adjusted were summarized in Supporting Information Text S3: Model Calibration.~~

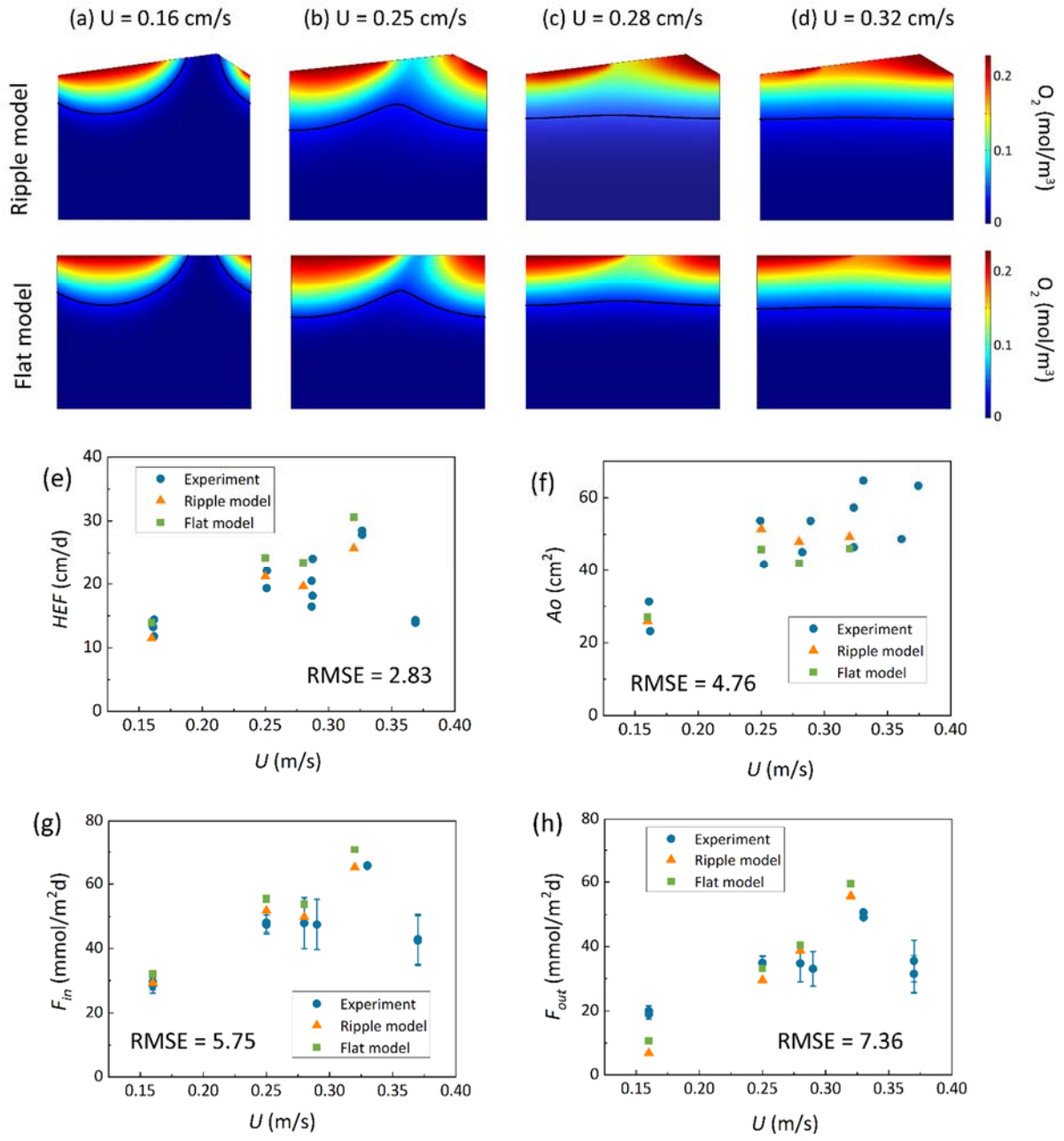

Figure 5. Comparison of numerical modeled oxygen distribution, (~~a~~e) hyporheic exchange flux, (~~b~~f) summed oxic zone and (~~c~~g) oxygen influx and (~~d~~h) oxygen outflux and experimental measurements by Wolke et al. (2020) under various conditions. The units of RMSE are (e) cm/d, (f) cm^2, (g) $mmol/m^2d$, and (h) $mmol/m^2d$.

For stationary and slow-migrating beds, the spatial distribution of oxygen creates a conchoidally shaped plume beneath the bedform; in contrast, beneath fast-migrating beds, the oxygen plume shifts to a more uniform front. The *HEF*, F_{in}, F_{out}, and A_O simulated using both

the ripple bedform model and the flat bed model were presented in Figure 5; these results are in good qualitative and quantitive agreement with the measurements of Wolke et al. (2020). The root means square error (RMSE) between the experimentally measured values and those simulated by the flat bed model were further calculated. All RMSE values fall within reasonable ranges, indicating the critical processes of bedform migration and oxygen dynamic are captured by the numerical models.

3.2 Effect of bedform migration on mixing and solute dynamic

To simulate the range of natural environmental conditions, the reactive transport equations were solved for different stream velocities, grain sizes and groundwater upwelling fluxes, which include a corresponding range of ripple migration celerites and sediment permeabilities derived from the empirical relations. As an example, the patterns of pore water transport as well as SW and GW mixing are shown for a grain size of 0.15 mm, a constant ratio between pumping driven hyporheic exchange flux and upwelling GW flux $U_b = 0.6$, and four different stream velocities, that is four different *Re* numbers.

For low surface water flow velocity (*Re* = 2500), no migration of bedform is predicted by the model. SW enters the riverbed layer in the high-pressure region on the stoss side, flows through the porous medium, and exits the riverbed layer in the low-pressure region on the lee side, forming a typical conchoidally shaped hyporheic flow cell. Upwelling GW is diverted around the hyporheic flow cell, mixes with SW, and then exits into the overlying water from both sides, in patterns similar to those shown previously by Fox et al. (2014) and Hester et al., (2019). SW and GW mixing zone (i.e. the mixing area where the fraction of GW ranges between 16% and 84%) emerges as a thin band along the hyporheic flow cell, and covers over 2.97% of

the modeled domain. Meanwhile, NMD denitrification occurs below the oxygen plume with the reactive zone in a conchoidal shaped distribution, while MD denitrification reactive zone develops along the edge of the mixing zone, where DOC from SW meets nitrate from GW (row 1 in Figure 6).

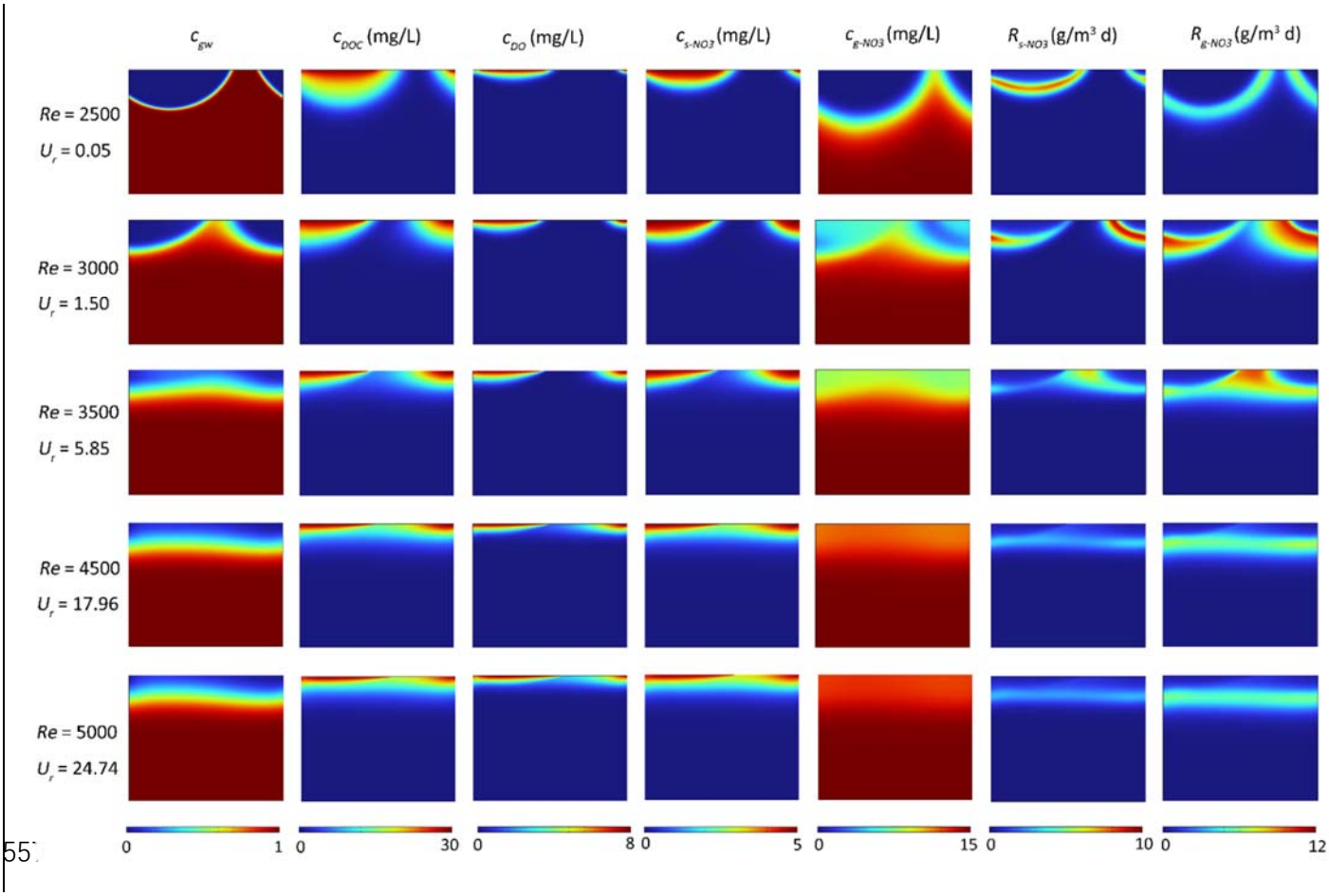

Figure 6. Effect of bedform migration on riverbed biogeochemistry for U_b = 0.6 and D_{50} = 0.15 mm. Shown are profiles of (column 1) conservation solute representing groundwater fraction (c_{gw}), (column 2) DOC concentration (c_{DOC}), (column 3) O_2 concentration (c_{DO2}), (column 4) s-NO_3^- concentration ($c_{s\text{-}NO3-}$), (column 5) g-NO_3^- concentration ($c_{g\text{-}NO3-}$), (column 6) non-mixing-dependent (NMD) denitrification rate ($R_{s\text{-}NO3-}$) and (column 7) mixing-dependent (MD) denitrification rate ($R_{g\text{-}NO3-}$).

564 At a surface water *Re* of 3000, bedforms migrate at a low celerity of 1.04 cm/h. This low
565 migration rate has minimal impact on the plumes of stream-borne O_2 and s-NO_3^-. The outflow
566 zone of groundwater-borne solutes (c_{gw} and g-NO_3^-) exhibits a slight upstream shift,
567 approaching the middle of the riverbed surface. The size of SW and GW mixing zone (GW
568 faction: 16%–84%) increases to 10.06% of the modeled domain. Furthermore, both the NMD
569 and MD denitrifying rates are enhanced at the start of bedform migration (row 2 in Figure 6).

570 With increasing stream velocity (*Re* = 3500), bedform migration drives continuous changes
571 in pressure distribution. The simulated hyporheic flow cells move downstream and decrease in
572 size at the same time. The shape of the SW and GW mixing zone changes distinctly, forming a
573 horizontal band with a wider range 10.71% of the whole domain (GW faction: 16%–84%). The
574 penetration of stream-derived solutes into the streambed is reduced, with a more gradual
575 concentration gradient in the horizontal and vertical directions, whereas the g-NO_3^- plume is
576 uniformly distributed horizontally. Both NMD and MD denitrification hot spots form in the
577 central position near the sediment-water interface as the bedform moving (row 3 in Figure 6).

578 When bedform migration is further increased (*Re* = 4500 and 5000), bedform migration
579 fully dominates over the pore water flow, and hence, continuous solute layers are found in the
580 subsurface (as depicted in row 4 and 5 of Figure 6). The penetration depths of stream-borne
581 solutes are decreased in comparison to those in slow- to medium- fast migrating bedforms. The
582 NMD and MD denitrification zones become thin and move upward with decreased reaction
583 rates. Similar to the conclusions obtained in previous studies (Kessler et al., 2015; Zheng et al.,
584 2019), bedform migration reduces the penetration depth of solute and the scope of hyporheic
585 exchange cell. We also found that bedform migration increases the size of mixing zone between

surface water and groundwater. The SW and GW mixing zone accounts for 9.30% and 9.14% of the domain area, respectively (take the GW fraction 16%–84% for example).

3.3 Effect of migration celerity on mixing regimes

The mixing intensity across the riverbed surface and the size of the mixing area within the subsurface were estimated by simulating four different grain sizes and five upwelling GW fluxes, under varying stream velocities associated with the corresponding bedform celerity. The evolutions of the hyporheic exchange flux, net mixing flux and size of mixing zone with increasing *Re* number were summarized in Figure 7. The 16–84% GW fraction range was displayed here to evaluate how migration celerity affects mixing regimes.

As shown in Figure 7, across various grain sizes, both *HEF* and *MF* increase with increasing stream velocity and bedform celerity. Nevertheless, the mixing fraction exhibits a significant increase at the onset of bedform migration, with a tendency to stabilize or decrease moderately as celerity further increases. This phenomenon is attributed to enhanced mixing between SW and discharging GW along the entire horizontal riverbed in moving bedforms—contrasting with stationary bedforms, where mixing occurs solely along the typical crescent-shaped hyporheic exchange flow cells (Figure 6). Additionally, when bedforms start moving and move at moderate velocities, the SW-GW mixing zone shows a significant increase compared to stationary ones. As bedform migration celerity accelerates, the extent of the mixing zone gradually approaches a plateau, with slight reductions observed at higher celerities.

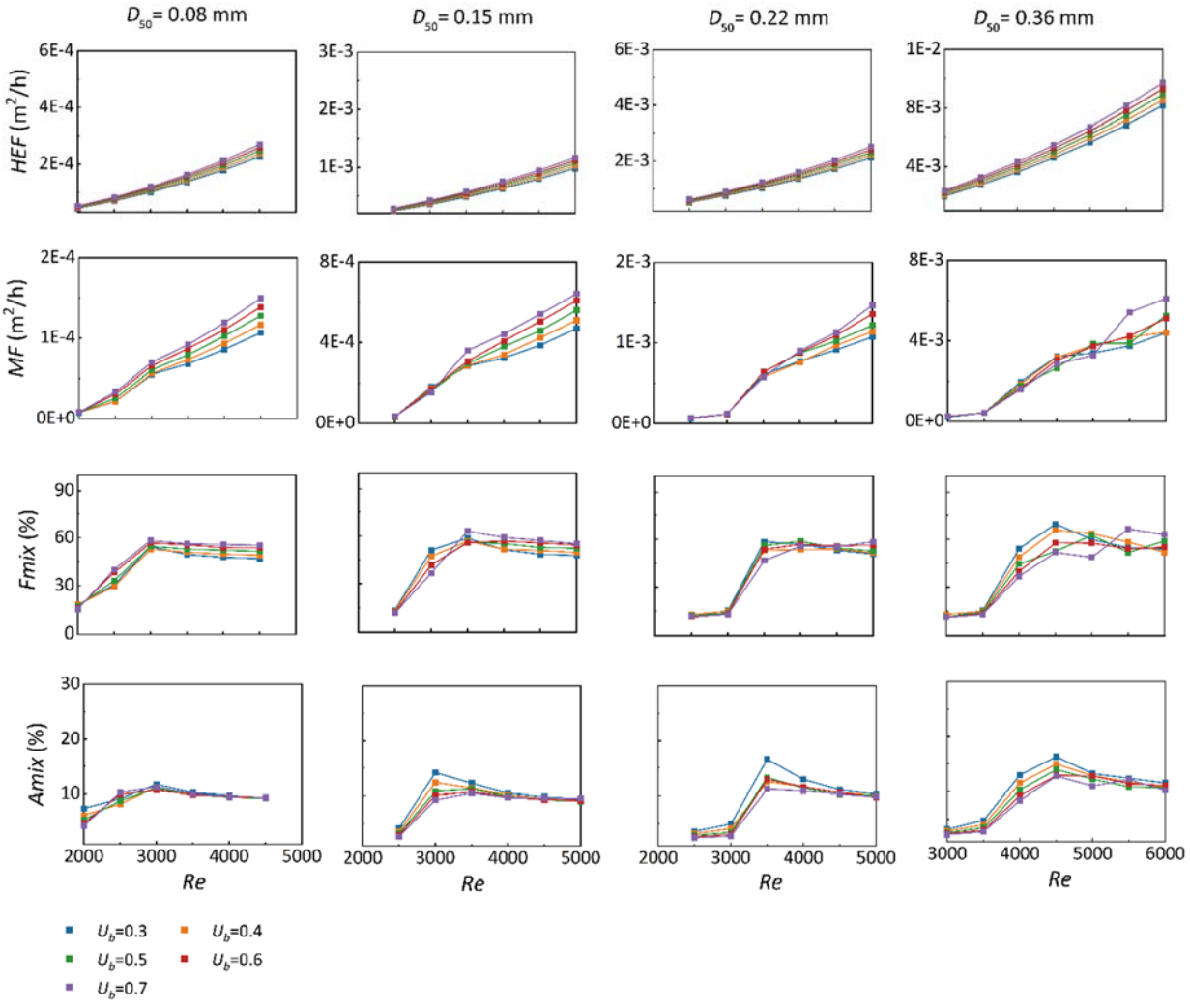

605

606 **Figure 7.** The variation of hyporheic exchange flux (*HEF*, row 1) and mixing flux (*MF*, row 2)
607 across the sediment-water interface, the proportion of mixing flux to hyporheic exchange flux
608 (*Fmix*, row 3) and the ratio of mixing zone to whole domain (*Amix*, row 4) with stream velocity
609 and associated bedform celerity across different medium grain size when U_b = 0.3−0.7.

610 Although the GW fraction range determines both mixing flux and scope, it does not alter
611 the effect of migration celerity on these mixing patterns. A broader groundwater fraction range
612 induces a larger mixing flux, an increased *Fmix*, and a wider mixing zone; nonetheless, *Amix*
613 persists as a relatively small scope (about 10–15% of the full domain) within the riverbed.
614 Relatively moderate differences in computed *MF* and *Fmix* are observed between the narrower

range (20–80%) and the baseline range (16–84%). For bedforms of different sediment grain sizes, *MF* represents around 60% of the total *HEF* when bedforms are moderately to fast-moving, compared with approximately 20% when they are stationary or slow-moving.

Taking a grain size of 0.15 mm and a constant ratio between pumping-driven hyporheic exchange flux and upwelling groundwater flux (U_b = 0.6) as an example, we varied α_L from 0.001 to 0.015 m (Figure S5). While increased longitudinal and transverse dispersivities clearly enhance *Fmix* and *Amix*, they do not modify the influence of bedform migration on these mixing metrics. This confirms that greater dispersivity enhances SW and GW mixing, leading to a larger proportion of hyporheic exchange flux involved in mixing and an expanded mixing zone. As such, reliable dispersion parameter estimates are essential for accurate mixing magnitude assessments. Additionally, *Fmix* and *Amix* values obtained under various GW fraction ranges and longitudinal and transverse dispersivities were presented in the Supporting Information (Text S4).

3.4 Impact of ripples migration on nitrate removal

To assess the impact of ripple migration on the removal of s-NO_3^- and g-NO_3^- within domains of varying medium grain sizes, the influx of nitrate into the riverbed layer and the total reaction rate within the riverbed layer were determined.

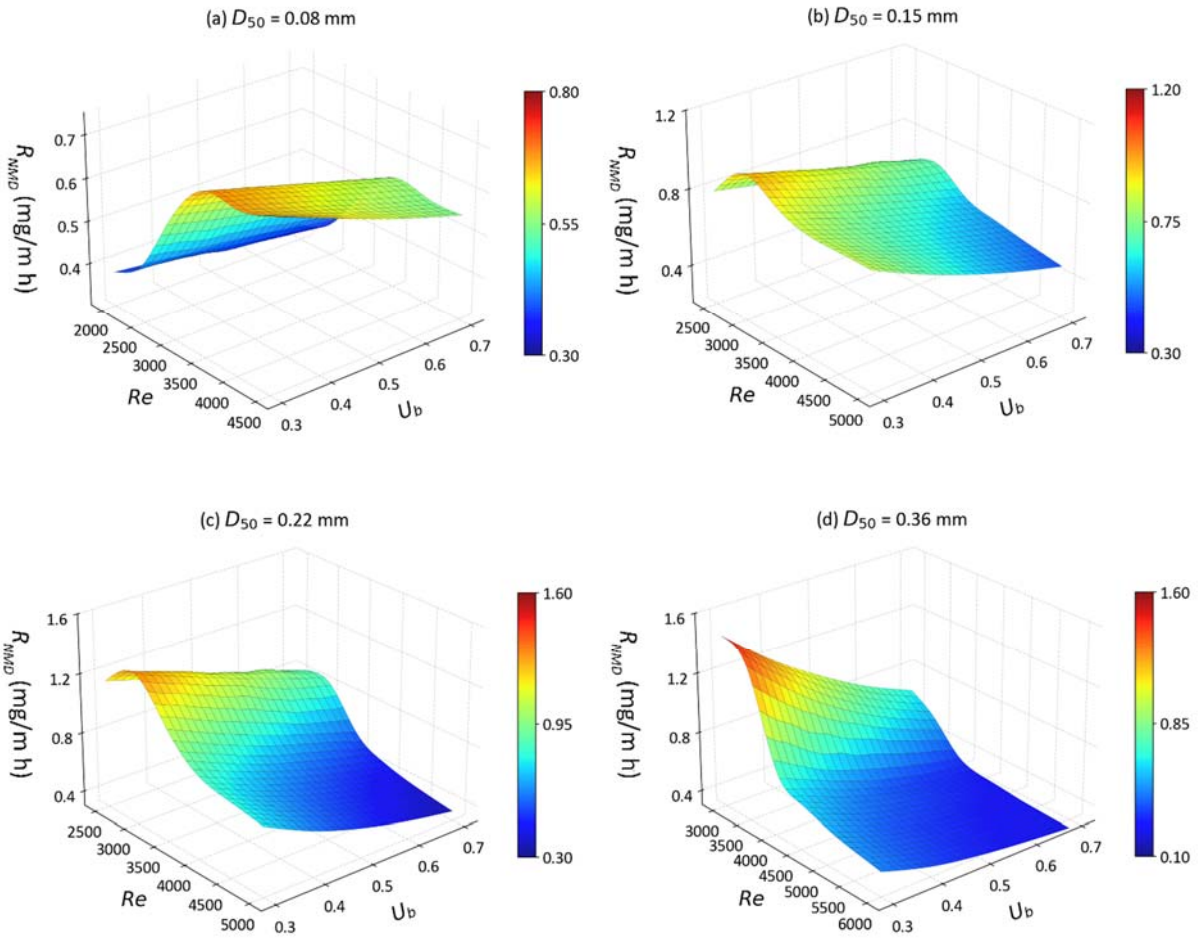

Figure 8. The non-mixing-dependent denitrification rates (R_{NMD}) as functions of U_b and Re for different medium grain sizes.

For s-NO_3^-, the NMD denitrification rate increases in moving bedforms composed of very fine sand (D_{50} = 0.08 mm). This is likely caused by higher flow velocities driving more reactants into the sediment, thereby enhancing denitrification in reaction-limited systems (Da > 2.97). In contrast, in riverbeds of fine to medium sand (D_{50} = 0.15−0.36 mm) with higher permeabilities, the rate of s-NO_3^- is negatively correlated with the mean stream velocity when the system becomes transport-limited (Da < 2). This is likely because s-NO_3^- travels fast along shorten flow paths and does not undergo denitrification within the moving bedforms (Figure 6). Additionally, the migrating bedforms enhance the delivery of s-NO_3^- into the sediment due to

increased *HEF*. Consequently, the removal efficiency of s-NO_3^- decreases monotonically across various medium grain sizes (Figure 9).

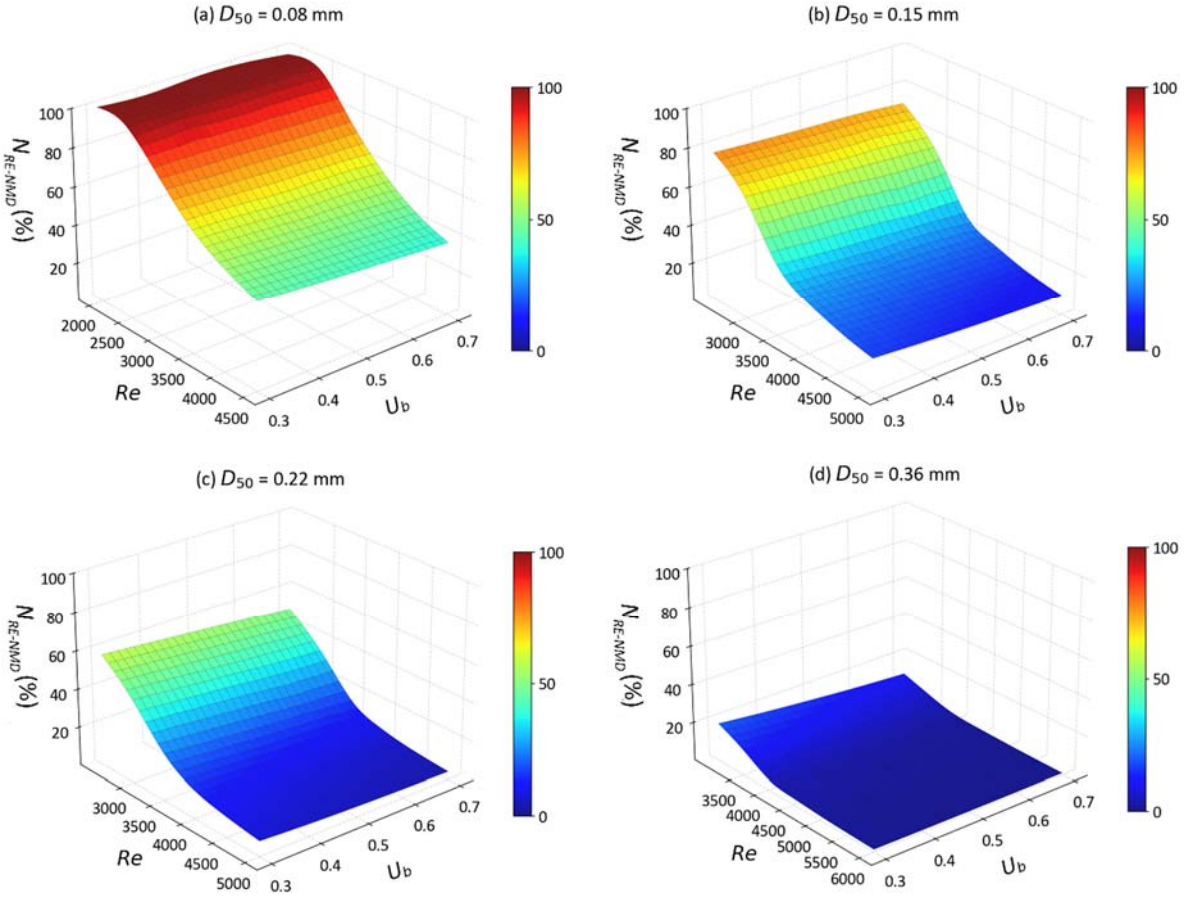

Figure 9. The removal efficiencies of stream borne nitrate ($N_{RE\text{-}NMD}$) as functions of U_b and *Re* for different medium grain sizes.

For g-NO_3^-, the increase in MD denitrification is also seen for fine sandy sediments (D_{50} = 0.08−0.22 mm) at low to medium *Re* (Figure 10). Compared to s-NO_3^-, the advective flow paths and residence times of g-NO_3^- in groundwater are longer. Additionally, the enhanced mixing dynamics between SW and GW further facilitates the occurrence of MD denitrification as the bedforms start moving. Consequently, the reduction rate of g-NO_3^- decreases only in riverbeds consisting of medium sand with fast bedform migration celerity (*Re* > 4000), as the solute residence time is significantly reduced. Interestingly, the rise in the MD denitrification rate

compensates for the increased g-NO_3^- influx in very fine sand (D_{50} = 0.08 and 0.15 mm) at moderate stream velocity (Re < 4000). Most of g-NO_3^- that enters the sediment is consumed before entering the overlying water column. For fine to medium sand riverbed, the g-NO_3^- removal efficiency decreases strongly with increasing Re. The natural protective role of the SW and GW mixing zone in preventing nitrate-contaminated GW from entering rivers is being hindered in fast moving bedforms (Figure 11).

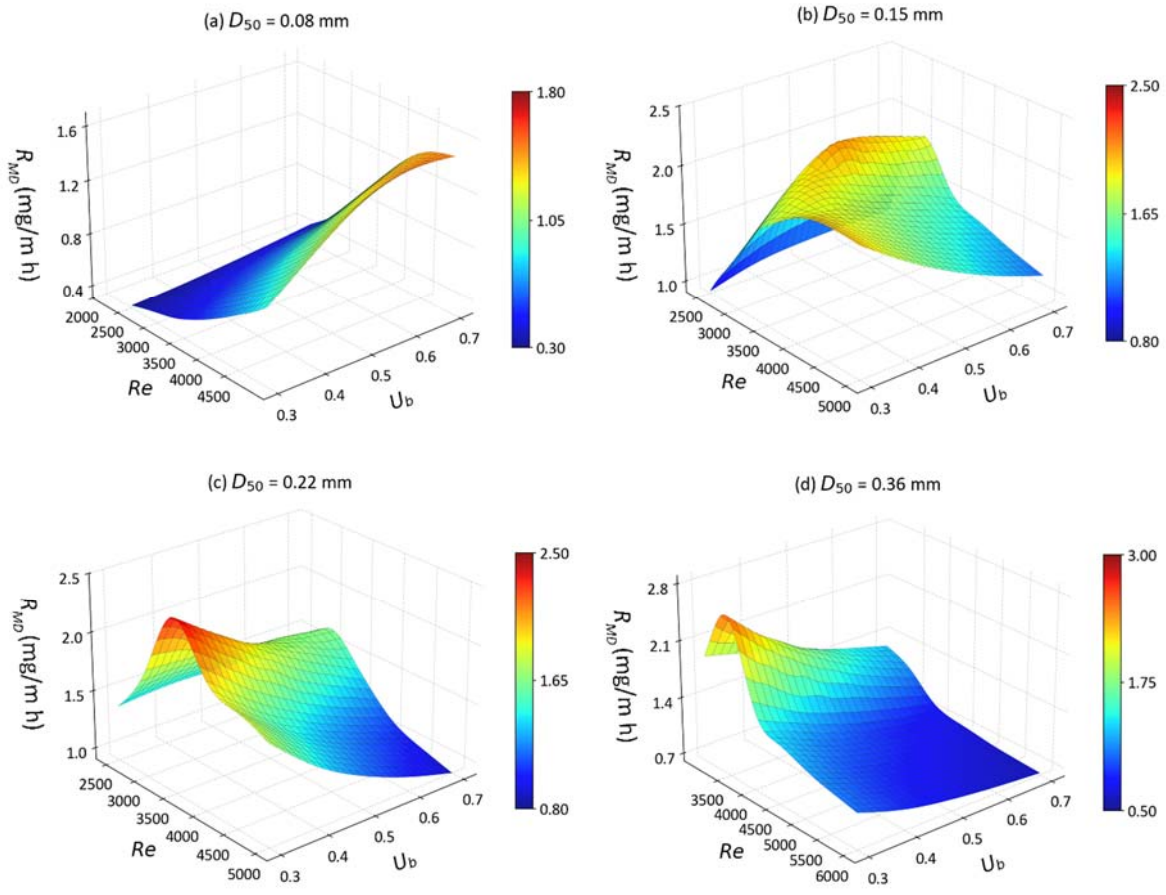

Figure 10. The mixing-dependent denitrification rates (R_{MD}) as functions of U_b and Re for different medium grain sizes.

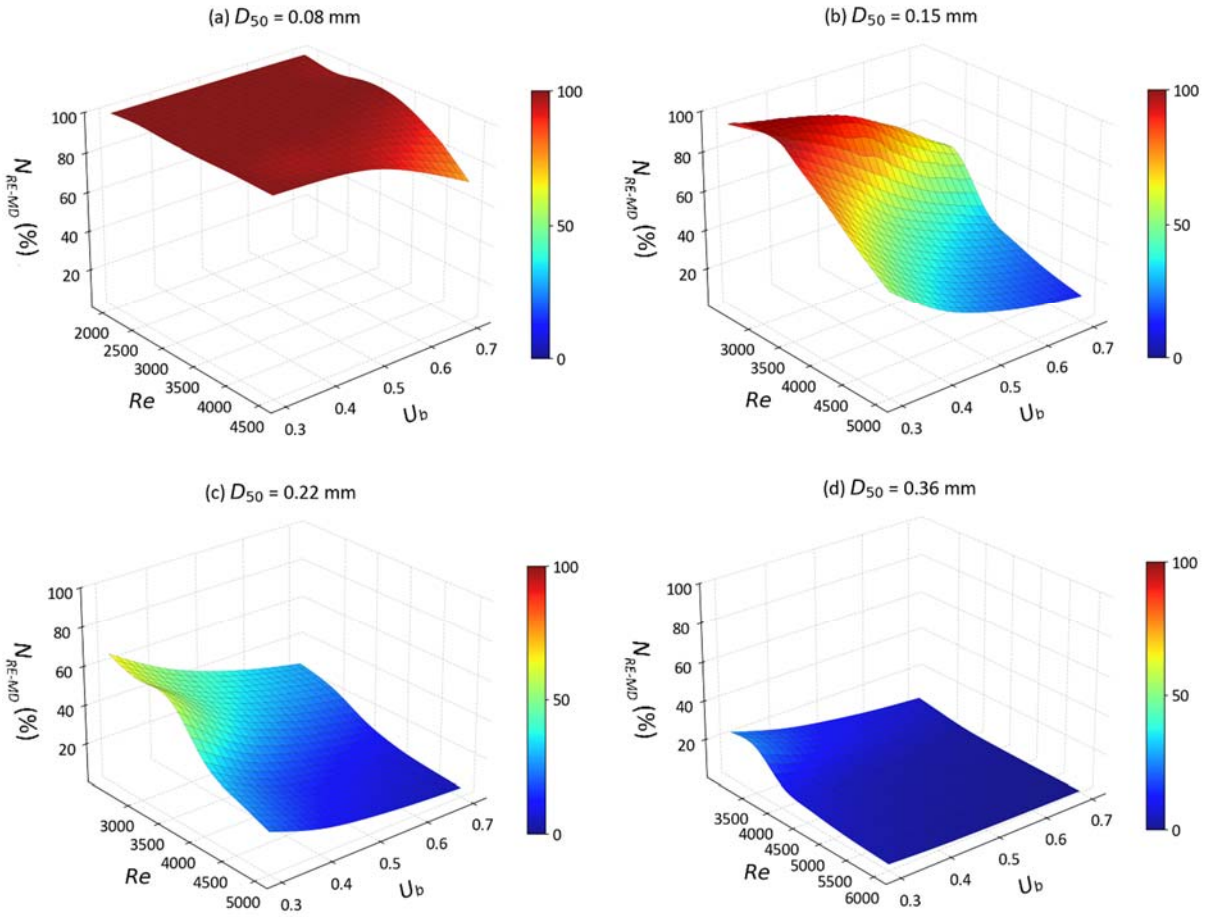

Figure 11. The removal efficiencies of groundwater borne nitrate ($N_{RE\text{-}MD}$) as functions of U_b and *Re* for different medium grain sizes.

4. Discussion

This study quantified the effect of bedform migration on SW and GW mixing process as well as mixing triggered denitrification. Previous research has primarily focused on the potential impacts of bedform migration on hyporheic exchange driven by streambed morphological features, as well as non-mixing-dependent biogeochemical processes where reactants are assumed to be predominantly in SW. However, such studies represent only a small subset of possible streambed environmental conditions, focusing exclusively on specific headwater stream conditions (Jiang et al., 2022; Kessler et al., 2015; Ping et al., 2022; Zheng et al., 2019). The

675 impact of bedform migration on the conceptual model of bedform-induced hyporheic exchange,
676 which is influenced by GW upwelling and/or ambient lateral GW flow in the mid-stream section
677 of lowland rivers, has received relatively less attention and examination.

678 In streams and rivers that are fed by regional GW and possess undulating bedforms, SW
679 gets mixed with GW throughout the local hyporheic exchange process. The mixing zone
680 exhibits a typical crescent shape along the periphery of typical hyporheic exchange cells within
681 a stationary streambed (as reported by Fox et al., 2014; Hester et al., 2019; Nogueira et al.,
682 2022). The sizes of the SW-GW mixing zone (e.g., thickness and area) occupy a small
683 proportion of the whole HZ. In the immobile bedform, the thin mixing zone occupying ~5% is
684 consistent with prior work (Hester et al., 2013; Santizo et al., 2020). However, at the onset of
685 bedform migration, the mixing pattern, extent, and intensity of SW-GW interactions are altered.
686 A continuous SW-GW mixing zone is formed within the ripples of the medium- to fast-moving
687 bedform (Figure 6), and the area of mixing zone increases to approximately 10 ~ 15% at this
688 time. Besides, the net flux of SW and GW mixing increases with stream velocity and bedform
689 migration celerity significantly (Figure 7). As a result, bedform migration controls and
690 determines the hotspots and magnitudes of the SW and GW mixing. The bedforms are typically
691 assumed to be immobile potentially making underestimations of SW-GW mixing flux and
692 mixing zone in a HZ.

693 Instead of the typical crescent-shaped MD denitrifying zone observed in stationary
694 bedforms (Naranjo et al., 2015; Hester et al., 2014, 2019), the MD reaction zonation changes to
695 the layer shape distributed at the fringe of the HEF cells, where mixing between SW and GW
696 develop to a largest degree (Figure 6). Such a situation exists where the stream flows into with a

relative homogeneous sandy riverbed with low autochthonous organic carbon content and encounters with nitrate enrich GW. The heterogeneous streambeds including buried autochthonous organic matter (Sawyer, 2015; Ping et al., 2022), deposited particulate organic particles (Drummond et al., 2017; Ping et al., 2023), and biological aggregate (Xian et al., 2022), would complicate the hyporheic exchange process, induce the rough and irregular shapes and boundaries of HEF cells and mixing zone, and therefore affect redox microenvironments and biogeochemical zonations. MD denitrifying hotspot would also develop around available sources of DOC.

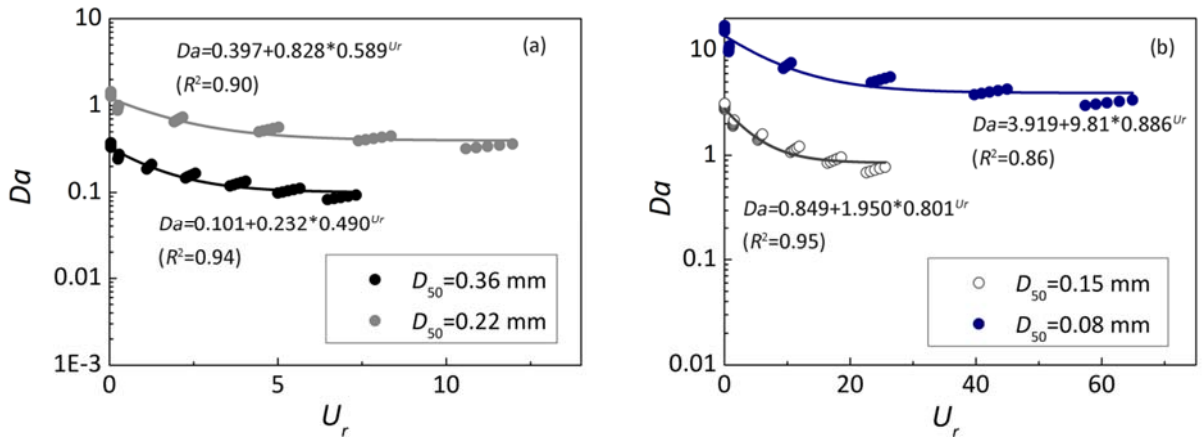

Figure 12. Variation of the dimensionless Damköhler number as a function of the dimensionless parameter U_r.

Previous studies have demonstrated that migrating bedforms constrains the penetration depths of stream-borne solute, shorten their transport timescale, and reduces the removal efficiency of stream-borne nitrate (Jiang et al., 2022; Kessler et al., 2015; Ping et al., 2022; Zheng et al., 2019). Our findings indicate that bedform migration exerts more complex influences on MD denitrification and groundwater-borne nitrate removal. Bedform migration facilitates increases in the MD denitrification rate, driven by enhanced mixing flux, a higher

714 mixing proportion, and an expanded mixing zone. At the same time, it shortens the residence
715 timescale of water and solutes, which is detrimental to the occurrence of denitrification. When
716 $Re < 4000$ (slow to moderate stream velocities), the MD denitrification rate of moving bedforms
717 is greater than or comparable to that of stationary bedforms; in contrast, for fast-moving
718 bedforms ($Re \geq 4000$), the MD denitrification rate decreases significantly. This is likely because
719 the reduction in MD rate driven by a shortened transport timescale dominates over the increase
720 caused by enhanced mixing intensity; meanwhile, at this stage (~*Re* 4000), the mixing fraction
721 of the total exchange flux and the extent of the mixing zone both approach plateaus. Fast-
722 moving bedforms also reduce the HZ attenuation capacity for groundwater-borne nitrate.
723 Notably, the g-NO_3^- removal efficiency in HZs peaks for stationary bedforms and those at the
724 onset of migration.

725 The causes of fast-moving bedforms' negative impact on g-NO_3^- removal differ depending
726 on the type of riverbed sediment (Figure 12). For very fine sand (D_{50} = 0.08 mm), a larger
727 celerity results in a decline in transport timescale with less impact on removal efficiency as the
728 system is rate-limited ($Da >> 1$). For fine to medium sand riverbed (D_{50} = 0.15–0.36 mm), the
729 transport-limited situation leads to a low denitrification rate with increasing U_r but constantly
730 decreasing *Da* ($Da < 1$). It is important to note that the calculated reaction timescale is based on
731 the consumption period of oxygen to a prescribed anoxic threshold. Under these conditions, the
732 exhaustion of labile DOC would also lead to the cessation of denitrification (Zarnetske et al.,
733 2011a, 2011b). These results demonstrate that in order to evaluate the self-purification capacity
734 of the HZ and its function as a natural barrier mitigating groundwater contamination, riverbed
735 sediment transport dynamics and grain size distributions need to be considered. Stabilizing

bedform configurations in restoration projects would enhance the natural attenuation capacity of HZs. Additionally, enhancing mixing intensity, along with extending the water residence timescale, would also facilitate the self-purification of HZs.

Different from previous studies that demonstrated the magnitude of NMD denitrification is often greater than that of MD denitrification (Hester et al., 2014; Trauth and Fleckenstein, 2017). The results in our study show that the total reaction rate of s-NO_3^- is smaller than that of g-NO_3^- in mobile bedforms. This phenomenon can be attributed to the following two reasons: First, the concentration of s-NO_3^- is one-third that of g-NO_3^-; Second, the reaction zone is reduced by migration celerity for NMD denitrification, while the reaction zone for MD denitrification is increased in the moving riverbed. Mixing intensity increases with bedform migration, a process that facilitates MD denitrification more effectively (Hester et al., 2019; Nogueira et al., 2024; Trauth and Fleckenstein., 2017). More attention should be paid to the mixing dynamics and mixing triggered biogeochemical reactions, which is helpful to put forward appropriate stream restoration plans so as to enhance the health of the aquatic ecosystem (Hester et al., 2017; Lawrence et al., 2013).

The findings of this study, derived from 2D numerical models, are most directly generalizable to straight, low-curvature streams with periodic bedform distributions in riverbed sediments. In such stream systems, hyporheic exchange is dominated by streamwise-vertical flow cells, with lateral (cross-stream) hyporheic flux accounting for a small fraction of total exchange (Hu et al., 2014; Naranjo et al., 2015). Importantly, straight, low-curvature streams are prevalent in agricultural and urban downstream gaining reaches, which are characterized by relatively homogeneous sediment types (e.g., fine sands). This is consistent with the focus of our

758 study, as these reaches often face nitrate pollution challenges and depend on natural attenuation
759 to maintain water quality (Hester et al., 2014; Trauth et al., 2017). In practice, riverbeds may
760 exhibit far more complex three-dimensional (3D) bedform morphologies coupled with sediment
761 heterogeneity, for example, in highly meandering streams (Gomez-Velez et al., 2017; Nogueira
762 et al., 2024; Pescimoro et al., 2019). Future studies should establish 3D numerical model and
763 incorporate stochastic hydraulic conductivity (K) fields to explore how sediment heterogeneity
764 interacts with bedform migration, evaluating whether high-K hotspots enhance or reduce
765 migration-driven mixing.

766 A critical limitation of this study is the reliance on empirical equations for bedform
767 migration celerity. The Chezy equation (suited for flat, homogeneous sediment beds) was used
768 to estimate the shear velocity for incipient sediment motion, with the experimentally derived
769 empirical relationship by Coleman and Melville (1994) further adopted to account for the
770 additional shear stress induced by ripples. The two-step approach (shear stress for particle
771 initiation and ripple-scale form drag via empirical formulations) reproduced Wolke's (2020)
772 results and proved useful for investigating the effects of bedform migration on hyporheic solute
773 transport (Ahmerkamp et al., 2017; Zheng et al., 2019). We did not simulate turbulent flow over
774 triangular bedforms nor compute shear stress via computational fluid dynamics (CFD; a
775 numerical method that would yield more precise pressure profiles and shear stress distributions)
776 given that the core focus of this study was to investigate how bedform migration affects
777 hyporheic solute transport and mixing-dependent denitrification within the riverbed layer. As
778 future work, the empirical approach should be validated using CFD simulations to enhance the
779 accuracy of bedform-related stress and migration calculations. This validation will facilitate the

quantification of potential uncertainties and refine the mechanistic understanding of bedform dynamic-hyporheic zone interactions.

This study focuses on ripples and, more broadly, shorter-wavelength topographic roughness elements formed under low subcritical flow conditions in sandy riverbeds (Ashley, 1990; Gomez-Velez et al., 2015; Raudkivi, 1997). The undulating bedforms maintain dynamic equilibrium through geometric adjustments, with their geometry remaining unchanged as the stream velocity fluctuates within a specific range (10–30 cm/s). When stream velocities exceed this upper threshold, a condition commonly observed in fast-flowing rivers, bedform geometries can be altered, ultimately leading to bedform erosion (Boano et al., 2013; Harvey et al., 2012). This process is not accounted for in the current model. If small-scale ripples develop and merge with larger-scale ripples and dunes under high stream velocities, the removal efficiency of s-NO_3^- and g-NO_3^- may be enhanced due to the extended hyporheic flow paths and increased residence timescales (Harvey et al., 2012; Zomer and Hoitink, 2024). Otherwise, the removal of s-NO_3^- would be highly hindered because of shorter residence time and fully oxic condition in fast moving bedforms and fast flowing rivers, while the removal of g-NO_3^- would likely be less affected within the immobile streambeds.

The numerical models assume isotropic sediment *K*. In fact, natural riverbeds with small-scale bedforms (e.g., dunes and ripples) commonly exhibit strong anisotropy. For bedforms with flow-transverse crests, pore pathways parallel to the crests are relatively continuous and straight yielding high transverse *K*. In contrast, pathways perpendicular to the crests are highly tortuous: water here must move upward through erosional, high-porosity troughs and downward over depositional, low-porosity crests. This undulating flow path, combined with flow separation and

local energy losses at morphological transitions, substantially increases hydraulic resistance and lowers longitudinal *K* (Dallmann et al., 2020; Salehin et al., 2004). Additionally, spatial variability in bedform dimensions (e.g., increasing dune wavelength downstream) enhances this anisotropy by introducing zones of differing flow resistance along the streamwise direction (Venditti et al., 2005). Given that the model is constructed along a longitudinal section with spatially consistent, periodic bedforms, the use of an isotropic hydraulic conductivity assumption is justified. Incorporating anisotropic *K* is critical for accurately modeling hyporheic exchange and related biogeochemical processes in 3D heterogeneous models.

DNRA was not incorporated in the model, given that denitrification is typically regarded as the predominant pathway for nitrate removal, whereas DNRA plays a secondary role in nitrate transformation (Zarnetske et al., 2012). Lansdown et al. (2012) and Quick et al. (2016) have demonstrated that approximately 5% of $^{15}NO_3^-$ tracer in river sediment incubations underwent DNRA, while 85% underwent denitrification. Nevertheless, DNRA competes with denitrification for NO_3^- and DOC as electron acceptor and donors within HZs. When an oligotrophic and/or a pristine stream infiltrate into the streambed and subsequently interact and mix with nitrate-enriched GW, the MD DNRA would not occur due to the low C/N ratio. When a eutrophication stream with higher DOC concentration, DNRA would have a greater influence in nitrate transformation because DNRA is prone to occur in NO_3^--limited (that is DOC sufficient) conditions compared to denitrification (Zhu et al., 2023). The ammonia produced by MD DNRA would be further nitrified within the aerobic HEF cell, thereby potentially elevating the risk of nitrate pollution in SW.

In this model, stream velocity and upward GW flux are considered constant in the present

model, yet they may change in time due to storm events, tidal pumping, snowmelt, or reservoir hydro-peaking (Liu et al., 2024; Nogueira et al., 2022; Song et al., 2018). Hester et al. (2019) demonstrated that increasing surface water stage would enhance both NMD and MD denitrification. Nogueira et al. (2024) and Trauth and Fleckenstein (2017) pointed out that GW discharge events increase the magnitude of SW-GW mixing, therefore effecting the prevalence of MD denitrification. The interactions among morphological dynamics, hyporheic exchange, and biogeochemical processes under transient conditions are key areas for future research.

5. Conclusion

The numerical model developed in this study was used to simulate the interaction and mixing of upwelling groundwater with bedform-induced hyporheic flow, examining how bedform migration influences SW and GW mixing and the processing of groundwater-borne nitrate within the HZ. Our analysis quantified the mixing flux and the size of mixing zone, as well as the mixing-dependent denitrification rates and removal efficiencies across riverbed sediments characterized by varying grain sizes, stream flow velocities, and groundwater discharge fluxes. These model simulations revealed that as bedforms migrate, the SW-GW mixing zone and the associated mixing-dependent denitrification zone progressively evolve into uniform, band-like structures. When turnover dominates the hyporheic exchange process, the mixing flux increases significantly (an increase of one order of magnitude). The mixing proportion of total exchange flux and mixing zone scope also experience significant increases at the onset of migration; as stream velocity further rises, the mixing proportion (~60%) and mixing size (~10–15% of the riverbed) gradually reach plateaus. Enhanced SW-GW mixing

dynamics facilitates MD denitrification as bedforms begins migration; however, shortened solute residence timescales resulting from fast bedform movement limits MD denitrification occurrence. Under dynamic bedform conditions, the self-purification capacity of the HZ is reduced for fine to medium sand (D_{50} = 0.15–0.36 mm), compromising its role as a natural barrier against groundwater contamination. Incorporating the identified and analyzed factors can enhance the management of riverbed sediment-associated aquatic systems, particularly for management objectives focused on removing groundwater-borne nitrate.

Supporting information

Additional details of the model scenarios and model validation were displayed in the supporting information.

Data availability

All raw data can be provided by the first author upon request.

Competing interest

The authors declare that they have no conflict of interest.

Author contribution

Conceptualization: XP, YX

Formal analysis: XP

Funding acquisition: XP, ZW, YX, SK

Investigation: XP, ZW

Methodology: XP, ZW, YX

Writing-original draft: XP

Writing-review and editing: ZW, YX, MJ, SK

Project administration: ZW

Acknowledgments

The work was financially supported by the National Natural Science Foundation of China (Nos. U23A2042, 42407075 and 42107089). This study was also supported by the Fellowship Program of China Postdoctoral Science Foundation under Grant Number 2025M773158 and GZC20241601, the "CUG Scholar" Scientific Research Funds at China University of Geosciences (Wuhan) (Project No.2023067), and. SK has been supported by the Royal Society (INF\R2\212060).

Reference

Ahmerkamp, S., Winter, C., Janssen, F., Kuypers, M. M., and Holtappels, M.: The impact of bedform migration on benthic oxygen fluxes, J. Geophys. Res.: Biogeosci. 120, 2229–2242, https://doi.org/10.1002/2015JG003106, 2015.

Ahmerkamp, S., Winter, C., Krämer, K., Beer, D. D., Janssen, F., Friedrich, J., Kuypers, M. M. M., and Holtappels, M.: Regulation of benthic oxygen fluxes in permeable sediments of the coastal ocean, Limnol. Oceanogr. 62(5), 1935–1954, http://doi.org/10.1002/lno.10544, 2017.

Ascott, M. J., Stuart, M. E., Gooddy, D. C., Marchant, B. P., Talbot, J. C., Surridge, B. J., and Polya, D. A.: Provenance of drinking water revealed through compliance sampling, Environ. Sci.: Processes & Impacts, 21(6), 1052-1064, https://doi.org/10.1039/C8EM00437D, 2019.

Ashley, G. M.: Classification of large-scale subaqueous bedforms: A new look at an old problem-SEPM bedforms and bedding structures, J. Sediment. Res. 60(1), 160–172, https://doi.org/10.1306/212F9138-2B24-11D7-8648000102C1865D, 1990.

Azizian, M., Grant, S. B., Kessler, A. J., Cook, P. L. M., Rippy, M. A., and Stewardson, M. J.: Bedforms as biocatalytic filters: a pumping and streamline segregation model for nitrate removal in permeable sediments, Environ. Sci. Technol. 49, 10993–11002, https://doi.org/10.1021/acs.est.5b01941, 2015.

Bardini, L., Boano, F., Cardenas, M. B., Revelli, R., and Ridolfi, L.: Nutrient cycling in bedform induced hyporheic zones, Geochim. Cosmochim. Acta, 84, 47–61, https://doi.org/10.1016/j.gca.2012.01.025, 2012.

Bartholdy, J., Ernstsen, V. B., Flemming, B. W., Winter, C., Bartholomä, A., and Kroon, A.: On the formation of current ripples, Sci. Rep. 5(1), 11390, https://doi.org/10.1038/srep11390, 2015.

Bear, J., and Verruijt, A.: Modeling groundwater flow and pollution. D. Reidel Publishing Company, 1998.

902 Boano, F., Harvey, J. W., Marion, A., Packman, A. I., Revelli, R., Ridolfi, L., and Wörman, A.:
903 Hyporheic flow and transport processes: Mechanisms, models, and biogeochemical
904 implications, Rev. Geophys. 52, 603–679, https://doi.org/10.1002/2012RG000417, 2014.

905 Boano, F., Poggi, D., Revelli, R., and Ridolfi, L.: Gravity-driven water exchange between
906 streams and hyporheic zones, Geophys. Res. Lett. 36, L20402,
907 https://doi.org/10.1029/2009GL040147, 2009.

908 Boano, F., Revelli, R., and Ridolfi, L.: Water and solute exchange through flat streambeds
909 induced by large turbulent eddies, J. Hydrol. 402, 290–296,
910 https://doi.org/10.1016/j.jhydrol.2011.03.023, 2011.

911 Boano, F., Revelli, R., and Ridolfi, L.: Modeling hyporheic exchange with unsteady stream
912 discharge and bedform dynamics, Water Resour. Res. 49(7), 4089–4099,
913 https://doi.org/10.1002/wrcr.20322, 2013.

914 Bottacin-Busolin, A., and Marion, A.: Combined role of advective pumping and mechanical
915 dispersion on time scales of bed form induced hyporheic exchange, Water Resour. Res. 46,
916 W08518, https://doi.org/10.1029/2009WR008892, 2010.

917 Boulton, A. J., Findlay, S., Marmonier, P., Stanley, E. H., and Valett, H. M.: The functional
918 significance of the hyporheic zone in streams and rivers, Annu. Rev. Ecol. Syst. 29(1), 59–
919 81, https://doi.org/10.1146/annurev.ecolsys.29.1.59, 1998.

920 Briggs, M. A., Lautz, L. K., Hare, D. K., and González-Pinzón, R.: Relating hyporheic fluxes,
921 residence times, and redox-sensitive biogeochemical processes upstream of beaver dams,
922 Freshw. Sci. 32, 622–641, https://doi.org/10.1899/12-110.1, 2013.

923 Burt, T. P., Howden, N. J. K., Worrall, F., Whelan, M. J., and Bieroza, M.: Nitrate in United
924 Kingdom rivers: Policy and its outcomes since 1970, Environ. Sci. Technol., 45(1), 175–
925 181, https://doi.org/10.1021/es101395s, 2011.

926 Cardenas, M. B.: Hyporheic zone hydrologic science: A historical account of its emergence and
927 a prospectus, Water Resour. Res. 51, 3601–3616, https://doi.org/10.1002/2015WR017028,
928 2015.

929 Cardenas, M. B., and Wilson, J. L.: The influence of ambient groundwater discharge on
930 exchange zones induced by current-bedform interactions, J. Hydrol. 331, 103–109,
931 https://doi.org/10.1016/j.jhydrol.2006.05.012, 2006.

932 Cardenas, M. B., Wilson, J. L., and Haggerty, R.: Residence time of bedform-driven hyporheic
933 exchange, Adv. Water Resour. 31(10), 1382–1386,
934 https://doi.org/10.1016/j.advwatres.2008.07.006, 2008.

935 Coleman, S. E., and Melville, B. W.: Bed-form development, J. Hydraul. Eng. 120(5), 544–560,
936 https://doi.org/10.1061/(ASCE)0733-9429(1994)120:5(544), 1994.

937 Conley, D. J., Paerl, H. W., Howarth, R. W., Boesch, D. F., Seitzinger, S. P., Havens, K. E.,
938 Lancelot, C., and Likens, G. E.: Ecology: controlling eutrophication: nitrogen and
939 phosphorus, Science 323, 1014–1015, https://doi.org/10.1126/science.1167755, 2009.

940 Dallmann, J., Phillips, C. B., Teitelbaum, Y., Sund, N., Schumer, R., Arnon, S., and Packman, A.
941 I.: Impacts of suspended clay particle deposition on sand-bed morphodynamics, Water
942 Resour. Res., 56(8), e2019WR027010, https://doi.org/10.1029/2019WR027010, 2020.

943 Drummond, J. D., Larsen, L. G., González-Pinzón, R., Packman, A. I., and Harvey, J. W.: Fine
944 particle retention within stream storage areas at base flow and in response to a storm event:
945 Particle retention stream storage areas, Water Resour. Res. 53, 5690–5705,
946 https://doi.org/10.1002/2016WR020202, 2017.

947 Elliott, A. H., and Brooks, N. H.: Transfer of nonsorbing solutes to a streambed with bed forms:
948 Theory, Water Resour. Res. 33(1), 123–136, https://doi.org/10.1029/96wr02784, 1997.

949 Fox, A., Boano, F., and Arnon, S.: Impact of losing and gaining streamflow conditions on
950 hyporheic exchange fluxes induced by dune-shaped bed forms, Water Resour. Res. 50(3),
951 1895–1907, https://doi.org/10.1002/2013WR014668, 2014.

952 Fox, A., Packman, A. I., Boano, F., Phillips, C. B., and Arnon, S.: (2018). Interactions between
953 suspended kaolinite deposition and hyporheic exchange flux under losing and gaining flow
954 conditions, Geophys. Res. Lett., 45(9), 4077–4085.
955 https://doi.org/10.1029/2018GL077951, 2018.

956 Gangi, A. F.: Permeability of unconsolidated sands and porous rocks, J. Geophys. Res. 90(B4),
957 3099–3104, https://doi.org/10.1029/JB090iB04p03099, 1985.

958 Gomez-Velez, J. D., Wilson, J. L., Cardenas, M. B., and Harvey, J. W.: Flow and residence times
959 of dynamic river bank storage and sinuosity-driven hyporheic exchange, Water Resour.
960 Res. 53, 8572–8595, https://doi.org/10.1002/2017WR021362, 2017.

961 Gomez-Velez, J. D., Harvey, J., Cardenas, M. B., and Kiel, B.: Denitrification in the Mississippi
962 River network controlled by flow through river bedforms, Nat. Geosci. 8, 941–975,
963 https://doi.org/10.1038/NGEO2567, 2015.

964 Gu, C., Hornberger, G. M., Herman, J. S., and Mills, A. L.: Effect of freshets on the flux of
965 groundwater nitrate through streambed sediments, Water Resour. Res. 44, W05415,
966 https://doi.org/10.1029/2007WR006488, 2008.

967 Harvey, J. W., Drummond, J. D., Martin, R. L., Mcphillips, L. E., Packman, A. I., Jerolmack, D.
968 J., Stonedahl, S. H., Aubeneau, A. F., Sawyer, A. H., and Larsen, L. G.:
969 Hydrogeomorphology of the hyporheic zone: Stream solute and fine particle interactions
970 with a dynamic streambed, J. Geophys. Res. 117(G4), G00N11,
971 https://doi.org/10.1029/2012JG002043, 2012.

972 Hedin, L. O., Von Fischer, J. C., Ostrom, N. E., Kennedy, B. P., Brown, M. G., and Robertson,
973 G. P.: Thermodynamic constraints on nitrogen transformations and other biogeochemical
974 processes at soil-stream interfaces, Ecology, 79(2), 684–703, https://doi.org/10.1890/0012-
975 9658(1998)079[0684:TCONAO]2.0.CO;2, 1998.

976 Hester, E. T., Cardenas, M. B., Haggerty, R., and Sourabh, S. V. A.: The importance and
977 challenge of hyporheic mixing, Water Resour. Res. 53, 3565–3575,
978 https://doi.org/10.1002/2016WR020005, 2017.

979 Hester, E. T., Eastes, L. A., and Widdowson, M. A.: Effect of surface water stage fluctuation on
980 mixing-dependent hyporheic denitrification in riverbed dunes, Water Resour. Res. 55,
981 4668–4687, https://doi.org/10.1029/2018WR024198, 2019.

982 Hester, E. T., Young, K. I., and Widdowson, M. A.: Mixing of surface and groundwater induced
983 by riverbed dunes: Implications for hyporheic zone definitions and pollutant reactions,
984 Water Resour. Res. 49, 5221–5237, https://doi.org/10.1002/wrcr.20399, 2013.

985 Hester, E. T., Young, K. I., and Widdowson, M. A.: Controls on mixing-dependent
986 denitrification in hyporheic zones induced by riverbed dunes: A steady state modeling
987 study, Water Resour. Res. 50, 9048–9066, https://doi.org/10.1002/2014WR015424, 2014.

988 Howden, N. J. K., and Burt, T. P.: Temporal and spatial analysis of nitrate concentrations from
989 the Frome and Piddle catchments in Dorset (UK) for water years 1978 to 2007: Evidence
990 for nitrate breakthrough? Sci. Total Environ. 407(1), 507–526,
991 http://doi.org/10.1016/j.scitotenv.2008.08.042, 2008.

992 Hu, H., Binley, A., Heppell, C. M., Lansdown, K., and Mao, X.: Impact of microforms on nitrate
993 transport at the groundwater-surface water interface in gaining streams, Adv. Water Resour.
994 73, 185–197, https://doi.org/10.1016/j.advwatres.2014.07.013, 2014.

995 Janssen, F., Cardenas, M. B., Sawyer, A. H., Dammrich, T., Krietsch, J., and de Beer, D.: A
996 comparative experimental and multiphysics computational fluid dynamics study of coupled
997 surface-subsurface flow in bed forms, Water Resour. Res. 48(8), W08514,
998 https://doi.org/10.1029/2012WR011982, 2012.

999 Jiang, Q., Liu, D., Jin, G., Tang, H., Wei, Q., and Xu, J.: N2O dynamics in the hyporheic zone
1000 due to ripple migration, J. Hydrol. 610, 127891,
1001 https://doi.org/10.1016/j.jhydrol.2022.127891, 2022.

1002 Kessler, A. J., Cardenas, M. B., and Cook, P. L. M.: The negligible effect of bed form migration
1003 on denitrification in hyporheic zones of permeable sediments, J. Geophys. Res.: Biogeosci.
1004 120, 538–548, https://doi.org/10.1002/2014JG002852, 2015.

Krause, S., Abbott, B. W., Baranov, V., Bernal, S., Blaen, P., Datry, T., Drummond, J., Fleckenstein, J. H., Velez, J. G., Hannah, D. M., Knapp, J. L. A., Kurz, M., Lewandowski, J., Martí, E., Mendoza-Lera, C., Milner, A., Packman, A., Pinay, G., Ward, A. S., and Zarnetzke, J. P.: Organizational principles of hyporheic exchange flow and biogeochemical cycling in river networks across scales, Water Resour. Res. 58 (3), e2021WR029771, https://doi.org/10.1029/2021WR029771, 2022.

Krause, S., Heathwaite, L., Binley, A., and Keenan, P.: Nitrate concentration changes at the groundwater-surface water interface of a small Cumbrian River, Hydrol. Processes, 23, 2195–2211, https://doi.org/10.1002/hyp.7213, 2009.

Krause, S., Tecklenburg, C., Munz, M., and Naden, E.: Streambed nitrogen cycling beyond the hyporheic zone: Flow controls on horizontal patterns and depth distribution of nitrate and dissolved oxygen in the upwelling groundwater of a lowland river, J. Geophys. Res.: Biogeosciences, 118, 54–67, https://doi.org/10.1029/2012JG002122, 2013.

Lansdown, K., Heppell, C. M., Dossena, M., Ullah, S., Heathwaite, A. L., Binley, A., Zhang, H., Trimmer, M., 2014. Fine-Scale in situ measurement of riverbed nitrate production and consumption in an armored permeable riverbed, Environ. Sci. Technol. 48 (8), 4425–4434, https://doi.org/10.1021/es4056005, 2014.

Lansdown, K., Heppell, C. M., Trimmer, M., Binley, A., Heathwaite, A. L., Byrne, P., and Zhang, H.: The interplay between transport and reaction rates as controls on nitrate attenuation in permeable, streambed sediments, J. Geophys. Res. Biogeosci. 120, 1093–1109, http://doi.org/10.1002/2014JG002874, 2015.

1026 Lansdown, K., Trimmer, M., Heppell, C. M., Sgouridis, F., Ullah, S., Heathwaite, L., Binley, A.,
1027 and Zhang, H.: Characterization of the key pathways of dissimilatory nitrate reduction and
1028 their response to complex organic substrates in hyporheic sediments, Limnol. Oceanogr. 57
1029 (2), 387– 400, https://doi.org/10.4319/lo.2012.57.2.0387, 2012.

1030 Lawrence, J. E., Skold, M. E., Hussain, F. A., Silverman, D. R., Resh, V. H., Sedlak, D. L.,
1031 Luthy, R. G., and McCray, J. E.: Hyporheic zone in urban streams: A review and
1032 opportunities for enhancing water quality and improving aquatic habitat by active
1033 management, Environ. Eng. Sci. 30, 480–501, https://doi.org/10.1089/ees.2012.0235, 2013.

1034 Liu, F., Ding, Y., Liu, J., Latif, J., Qin, J., Tian, S., Sun, S., Guan, B., Zhu, K., and Jia, H.: The
1035 effect of redox fluctuation on carbon mineralization in riparian soil: An analysis of the
1036 hotspot zone of reactive oxygen species production, Water Res. 265, 122294,
1037 https://doi.org/10.1016/j.watres.2024.122294, 2024.

1038 Liu, Y., Liu, C., Nelson, W. C., Shi, L., Xu, F., Liu, Y., ... and Zachara, J. M.: Effect of water
1039 chemistry and hydrodynamics on nitrogen transformation activity and microbial
1040 community functional potential in hyporheic zone sediment columns, Environ. Sci.
1041 Technol., 51(9), 4877–4886, https://doi.org/10.1021/acs.est.6b05018, 2017.

1042 Marzadri, A., Tonina, D., and Bellin, A.: Morphodynamic controls on redox conditions and on
1043 nitrogen dynamics within the hyporheic zone: application to gravel bed rivers with
1044 alternate-bar morphology, J. Geophys. Res.: Biogeosci. 117, 184–189,
1045 https://doi.org/10.1029/2012JG001966, 2012.

1046 Monod, J.: The growth of bacteria cultures, Annu. Rev. Microbiol., 3, 371–394,
1047 https://doi.org/10.1146/annurev.mi.03.100149.002103, 1949.

1048 Munz, M., Krause, S., Tecklenburg, C., and Binley, A.: Reducing monitoring gaps at the aquifer-
1049 river interface by modelling groundwater-surface water exchange flow patterns, Hydrol.
1050 Processes, 25, 3547–3562, https://doi.org/10.1002/hyp.8080, 2011.

1051 Naranjo, R. C., Niswonger, R. G., and Davis, C. J.: Mixing effects on nitrogen and oxygen
1052 concentrations and the relationship to mean residence time in a hyporheic zone of a riffle-
1053 pool sequence, Water Resour. Res. 51(9), 7202–7217,
1054 https://doi.org/10.1002/2014WR016593, 2015.

1055 Nogueira, G. E. H., Partington, D., Heidbuchel, I., and Fleckenstein, J. H.: Combined effects of
1056 geological heterogeneity and discharge events on groundwater and surface water mixing, J.
1057 Hydrol. 638, 131467, https://doi.org/10.1016/j.jhydrol.2024.131467, 2024.

1058 Nogueira, G. E. H., Schmidt, C., Brunner, P., Graeber, D., and Fleckenstein, J. H.: Transit-time
1059 and temperature control the spatial patterns of aerobic respiration and denitrification in the
1060 riparian zone, Water Resour. Res. 57 (12), e2021WR030117,
1061 https://doi.org/10.1029/2021WR030117, 2021.

1062 Nogueira, G. E. H., Schmidt, C., Partington, D., Brunner, P., and Fleckenstein, J. H.:
1063 Spatiotemporal variations in water sources and mixing spots in a riparian zone, Hydrol.
1064 Earth Syst. Sci, 26 (7), 1883–1905, https://doi.org/10.5194/hess-26-1883-2022, 2022.

1065 Ocampo, C. J., Oldham, C. E., and Sivapalan, M.: Nitrate attenuation in agricultural catchments:
1066 shifting balances between transport and reaction, Water Resour. Res. 42(1), 85–88,
1067 https://doi.org/10.1029/2004WR003773, 2006.

1068 Peleg, E., Teitelbaum, Y., and Arnon, S.: Exploring the influence of sediment motion on
1069 microplastic deposition in streambeds, Water Res. 249, 120952,
1070 https://doi.org/10.1016/j.watres.2023.120952, 2024.

1071 Pescimoro, E., Boano, F., Sawyer, A. H., and Soltanian, M. R.: Modeling influence of sediment
1072 heterogeneity on nutrient cycling in streambeds, Water Resour. Res. 55,
1073 https://doi.org/10.1029/2018WR024221, 2019.

1074 Ping, X., Xian, Y., and Jin, M.: Influence of bedform migration on nitrate reduction in hyporheic
1075 zones of heterogeneous sediments, Water Resour. Res. 58, e2022WR033258,
1076 https://doi.org/10.1029/2022WR033258, 2022.

1077 Ping, X., Xian, Y., and Jin, M.: Effect of particulate organic carbon deposition on nitrate
1078 reduction in the hyporheic zone, Water Resour. Res. 59, e2022WR034253,
1079 https://doi.org/10.1029/2022WR034253, 2023.

1080 Precht, E., Franke, U., Polerecky, L., and Huttel, M.: Oxygen dynamics in permeable sediments
1081 with wave-driven pore water exchange, Limnol. Oceanogr. 49(3), 693–705,
1082 https://doi.org/10.2307/3597786, 2004.

1083 Quick, A. M., Reeder, W. J., Farrell, T. B., Tonina, D., Feris, K. P., and Benner, S. G.: Controls
1084 on nitrous oxide emissions from the hyporheic zones of streams, Environ. Sci. Technol. 50
1085 (21), 11491–11500, https://doi.org/10.1021/acs.est.6b02680, 2016.

Raudkivi, A. J.: Ripples on stream bed, J. Hydraul. Eng. 123(1), 58–64, https://doi.org/10.1061/(ASCE)0733-9429(1997)123:1(58), 1997.

Reeder, W. J., Quick, A. M., Farrell, T. B., Benner, S. G., Feris, K. P., and Tonina, D.: Spatial and temporal dynamics of dissolved oxygen concentrations and bioactivity in the hyporheic zone, Water Resour. Res. 54, 2112–2128, https://doi.org/10.1002/2017WR021388, 2018.

Risse-Buhl, U., Arnon, S., Bar-Zeev, E., Oprei, A., Packman, A. I., Peralta-Maraver, I., Robertson, A., Teitelbaum, Y., and Mutz, M.: Streambed migration frequency drives ecology and biogeochemistry across spatial scales, Wiley Interdiscip. Rev.: Water, 10. https://doi.org/10.1002/wat2.1632, 2023.

Rivett, M. O., Buss, S. R., Morgan, P., Smith, J. W. N., and Bemment, C. D.: Nitrate attenuation in groundwater: A review of biogeochemical controlling processes, Water Res. 42, 4215–4232, http://doi.org/10.1016/j.watres.2008.07.020, 2008.

Roche, K. R., Blois, G., Best, J. L., Christensen, K. T., Aubeneau, A. F., and Packman, A. I.: Turbulence links momentum and solute exchange in coarse-grained streambeds, Water Resour. Res. 54, 3225–3242, https://doi.org/10.1029/2017WR021992, 2018.

Roche, K. R., Li, A., Bolster, D., Wagner, G. J., and Packman, A. I.: Effects of turbulent hyporheic mixing on reach-scale transport, Water Resour. Res. 55, https://doi.org/10.1029/2018WR023421, 2019.

Rouse, J. D., Bishop, C. A., and Struger, J.: Nitrogen pollution: an assessment of its threat to amphibian survival, Environ. Health Perspect. 107, 799–803, https://doi.org/10.1289/ehp.99107799, 1999.

1107 Salehin, M., Packman, A. I., and Paradis, M.: Hyporheic exchange with heterogeneous
1108 streambeds: Laboratory experiments and modeling, Water Resour. Res. 40, W11504,
1109 http://doi.org/10.1029/2003WR002567, 2004.

1110 Santizo, K. Y., Widdowson, M. A., and Hester, E. T.: Abiotic mixing-dependent reaction in a
1111 laboratory simulated hyporheic zone, Water Resour. Res. 56 (9), e2020WR027090,
1112 https://doi.org/10.1029/2020WR027090, 2020.

1113 Sawyer, A. H.: Enhanced removal of groundwater-borne nitrate in heterogeneous aquatic
1114 sediments, Geophys. Res. Lett. 42(2), 403–410, https://doi.org/10.1002/2014GL062234,
1115 2015.

1116 Schindler, R. J., Parsons, D. R., Ye, L., Hope, J. A., Baas, J. H., Peakall, J., Manning, A. J.,
1117 Aspden, A. J., Malarkey, J., and Simmons, S.: Sticky stuff: redefining bedform prediction
1118 in modern and ancient environments, Geology, 43, 399–402,
1119 https://doi.org/10.1130/G36262.1, 2015.

1120 Schulz, H., Teitelbaum, Y., Lewandowski, J., Singer, G. A., and Arnon, S.: Moving bedforms
1121 control CO2 production and distribution in sandy river sediments, J. Geophys. Res.:
1122 Biogeosci. 128, e2022JG007156, https://doi.org/10.1029/2022JG007156, 2023.

1123 Shelley, F., Klaar, M., Krause, S., and Trimmer, M.: Enhanced hyporheic exchange flow around
1124 woody debris does not increase nitrate reduction in a sandy streambed, Biogeochem. 136
1125 (3), 353-372, https://doi.org/10.1007/s10533-017-0401-2, 2017.

1126 Soulsby, R.: Dynamics of marine sands: a manual for practical applications, Oceanogr. Lit. Rev.,
1127 9, 947, 1997.

1128 Song, X., Chen, X., Stegen, J., Hammond, G., Song, H.-S., Dai, H., Graham, E., and Zachara, J.
1129 M.: Drought conditions maximize the impact of high-frequency flow variations on thermal
1130 regimes and biogeochemical function in the hyporheic zone, Water Resour. Res. 54 (10),
1131 7361–7382, https://doi.org/10.1029/2018WR022586, 2018.

1132 Stelzer, R. S., and Bartsch, L. A.: Nitrate removal in deep sediments of a nitrogen-rich river
1133 network: A test of a conceptual model, J. Geophys. Res. 117, G02027,
1134 http://doi.org/10.1029/2012JG001990, 2012.

1135 Tonina, D., and Buffington, J. M.: Hyporheic exchange in gravel bed rivers with pool-riffle
1136 morphology: Laboratory experiments and three-dimensional modeling, Water Resour. Res.
1137 43, W01421, https://doi.org/10.1029/2005WR004328, 2007.

1138 Trauth, N., and Fleckenstein, J. H.: Single discharge events increase reactive efficiency of the
1139 hyporheic zone, Water Resour. Res. 53(1), 779–798.
1140 https://doi.org/10.1002/2016WR019488, 2017.

1141 Trauth, N., Musolff, A., Knller, K., Kaden, U. S., and Fleckenstein, J. H.: River water infiltration
1142 enhances denitrification efficiency in riparian groundwater, Water Resour. 130, 185–199,
1143 https://doi.org/10.1016/j.watres.2017.11.058, 2017.

1144 Venditti, J. G., Church, M., and Bennett, S. J.: Morphodynamics of small-scale superimposed
1145 sand waves over migrating dune bed forms, Water Resour. Res., 41(10), W10423,
1146 https://doi.org/10.1029/2004WR003461, 2005.

Wolke, P., Teitelbaum, Y., Deng, C., Lewandowski, J., and Arnon, S.: Impact of bed form celerity on oxygen dynamics in the hyporheic zone, Water, 12(1), 62, https://doi.org/10.3390/w12010062, 2020.

Wondzell, S. M., LaNier, J., Haggerty, R., Woodsmith, R. D., and Edwards, R. T.: Changes in hyporheic exchange flow following experimental wood removal in a small, low-gradient stream, Water Resour. Res. 45, https://doi.org/10.1029/2008WR007214, 2009.

Woessner, W.: Stream and fluvial plain ground water interactions: rescaling hydrogeologic thought, Ground Water, 38(3), 15–25, https://doi.org/10.1111/j.1745-6584.2000.tb00228.x, 2000.

Wu, L., Gomez-Velez, J. D., Li, L., and Carroll, K. C.: The fragility of bedform-induced hyporheic zones: Exploring impacts of dynamic groundwater table fluctuations, Water Resour. Res. 60, e2023WR036706, https://doi.org/10.1029/2023WR036706, 2024.

Xian, Y., Jin, M., Zhan, H., and Liang, X.: Permeable biofilms can support persistent hyporheic anoxic microzones, Geophys. Res. Lett. 49, e2021GL096948, https://doi.org/10.1029/2021GL096948, 2022.

Zarnetske, J. P., Haggerty, R., Wondzell, S. M., and Baker, M. A.: Dynamics of nitrate production and removal as a function of residence time in the hyporheic zone, J. Geophys. Res. Biogeosci. 116, G01025, https://doi.org/10.1029/2010JG001356, 2011a.

Zarnetske, J. P., Haggerty, R., Wondzell, S. M., and Baker, M. A.: Labile dissolved organic carbon supply limits hyporheic denitrification, J. Geophys. Res. Biogeosci. 116, G04036, https://doi.org/10.1029/2011JG001730, 2011b.

1168 Zarnetske, J. P., Haggerty, R., Wondzell, S. M., Bokil, V. A., and González-Pinzón, R.: Coupled
1169 transport and reaction kinetics control the nitrate source-sink function of hyporheic zones,
1170 Water Resour. Res. 48 (11), 1–15, https://doi.org/10.1029/2012WR011894, 2012.

1171 Zheng, L., Cardenas, M. B., Wang, L., and Mohrig, D.: Ripple effects: Bed form
1172 morphodynamics cascading into hyporheic zone biogeochemistry, Water Resour. Res. 55,
1173 7320–7342, https://doi.org/10.1029/2018WR023517, 2019.

1174 Zhu, Y., Dai, H., and Yuan, S.: The competition between heterotrophic denitrification and
1175 DNRA pathways in hyporheic zone and its impact on the fate of nitrate, J. Hydrol. 626:
1176 130175, https://doi.org/10.1016/j.jhydrol.2023.130175, 2023.

1177 Zomer, J. Y., and Hoitink, A. J. F.: Evidence of secondary bedform controls on river dune
1178 migration, Geophys. Res. Lett. 51(15), https://doi.org/10.1029/2024GL109320, 2024.